Progress In Electromagnetics Research B, Vol. 88, 151–173, 2020

Physical Optics Scattering by a PEC Plate Located Vertically over a Dielectric Half-space

Burak Polat* and Ramazan Daşbaşı

Abstract—Analytical solution and numerical results are provided for the problem of plane wave scattering by an electrically large Perfect Electric Conductor plate located vertically over a simple lossy dielectric half-space. The incoming monochromatic homogeneous plane wave is assumed to be incident from an arbitrary direction and decomposed into TE and TM components. Physical Optics approximation is used for estimating the currents induced on the plate. The scattered fields are obtained explicitly by evaluating the Electric Field Integral Equation analytically incorporating the set of Green functions by R. W. P. King which apply under High Contrast Approximation. Amplitude and phase variations of the numerical distance and attenuation function are illustrated in HF-MW band ranges. Azimuth and elevation patterns for scattered electric fields are illustrated with emphasis on the relative contributions of surface wave fields depending on operating frequency and refractivity. An analytical procedure to extract free space RCS information from measured/calculated data is introduced based on the asymptotic behaviors of surface waves and its stability is tested numerically.

1. INTRODUCTION

Electromagnetic waves generated due to Hertzian dipoles radiating in a transmissive medium comprising two simple half-spaces have complicated behaviors. In literature radiation mechanisms falling into this category are called *Sommerfeld Problems*. Interested readers are referred to recent papers by Michalski et al. (see especially [1–4] and the references therein) for a comprehensive review and recent advances on the topic. The point source induces surface waves localized in the close neighborhood of the interface with sophisticated amplitude and phase behaviors described by a special class of complex valued error functions. Compared to the space waves that decay algebraically in the radial direction with r^{-1} in the far field, the surface waves may decay as ρ^{-1}, ρ^{-2} or $e^{-\beta\rho}\sqrt{\rho}$ along the ground (as illustrated in Fig. 5), as they additionally display an exponential decay in the perpendicular direction. The surface waves play the leading role in transportation of energy over the ground to large distances (even over the horizon) in HF band. On the other hand, in VHF and upper band applications their contribution to total radiated/scattered far field is generally neglected since the transmitter (Tx) or the receiver (Rx) is generally air-based (i.e., located at sufficiently high altitude electrically) or quite far to the scatterer so that the surface wave contribution diminishes (cf. [5–8]). When both Tx and Rx are located close to the air-ground interface, this argument drops and analytical (parametric) investigation of the relative contributions of surface waves (as compared to geometrical optics (GO) fields) become determinative.

The motivation of the present canonical problem is to take the first step toward full wave investigation of scattering by electrically large vehicles and platforms located over a simple lossy dielectric half space. The features of our investigation are as follows:

Received 28 May 2020, Accepted 3 September 2020, Scheduled 23 September 2020
* Corresponding author: Burak Polat (abpolat@yildiz.edu.tr).
The authors are with the Department of Electronics and Communications Engineering, Yildiz Technical University, Istanbul, Turkey.

(i) The scatterer is picked as a rectangular Perfect Electric Conductor (PEC) plate positioned vertically with the bottom rim located on the interface. When the bottom rim of the plate is raised up into the air, multiple interaction mechanism between the interface and the rims intensifies. At this point one may mention to a number of GO and Physical Optics (PO) based ray tracing techniques in literature such as "four path model" or "shooting and bouncing ray" (cf. [6, 9, 10]) which work (only) with space waves for modeling multiple interaction mechanisms.

(ii) The electrical width and height of the PEC plate are assumed sufficiently large so that PO approximation in the Far Field Electric Field Integral Equation (FF-EFIE) approximates the induced currents successfully.

The investigation starts with decomposing the incoming monochromatic homogeneous plane wave into TE and TM components. Next, the PO currents induced on the plate and the necessary Cartesian Green dyadics that constitute the FF-EFIE are provided. This is followed with introduction of an analytical approach to extract free space Radar Cross Section (RCS) information from measured/calculated data over both planar and spherical grounds and its stability is tested numerically through HF-MW bands. Time dependence $\exp(-i\omega t)$ is assumed and suppressed.

2. FORMULATION

We consider the scenario in Fig. 1. The constitutive parameters of upper (air) and lower (simple lossy dielectric) half-spaces are denoted by (ε_0, μ_0) and $(\varepsilon, \mu_0, \sigma)$ with wave numbers $k = \omega\sqrt{\mu_0\,\varepsilon_0}$ and $k_1 = Nk$. The refractivity is given by $N = \sqrt{\varepsilon_r^c}$, where $\varepsilon_r^c = \varepsilon_r(1 + i\tau)$ is the complex relative permittivity; $\varepsilon_r = \varepsilon/\varepsilon_0$ is the relative permittivity; and $\tau = \frac{\sigma}{\omega\varepsilon} = \frac{18\sigma_{\mathrm{S/m}}}{\varepsilon_r f_{\mathrm{GHz}}}$ is called tangent loss. The real and imaginary parts of refractivity can be expressed explicitly by

$$\Re\{N\} = \sqrt{\frac{\varepsilon_r}{2}\left[1 + \sqrt{1+\tau^2}\right]} > 0, \quad \Im\{N\} = \sqrt{\frac{\varepsilon_r}{2}\left[-1 + \sqrt{1+\tau^2}\right]} \geq 0.$$

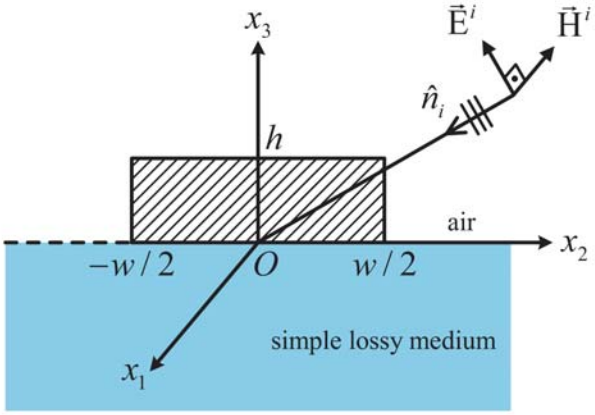

Figure 1. The geometry of the problem.

The plate is located on $S = \{(x_1, x_2, x_3) | x_1 = 0,\ x_2 \in [-w/2, w/2],\ x_3 \in [0, h]\}$ in the reference frame $Ox_1x_2x_3$. A uniform monochromatic plane wave propagating in the direction $\hat{n}_i = -\hat{r}(\theta_i, \phi_i) = -\hat{\rho}(\phi_i)\sin\theta_i - \hat{x}_3\cos\theta_i$ with $\hat{\rho}(\phi_i) = \hat{x}_1\cos\phi_i + \hat{x}_2\sin\phi_i$, $\phi_i \in (-\pi, \pi]$ is incident on the plate. The fields of the incoming wave are related by

$$\vec{H}^i = \frac{1}{Z}\hat{n}_i \times \vec{E}^i \ \text{ or } \ \vec{E}^i = Z\,\vec{H}^i \times \hat{n}_i$$

with

$$\vec{E}^i = \left[\hat{\theta}(\theta_i, \phi_i)E_{\theta 0} + \hat{\phi}(\phi_i)E_{\phi 0}\right] e^{i\vec{k}_i\cdot\vec{r}}, \quad \vec{H}^i = \left[\hat{\theta}(\theta_i, \phi_i)H_{\theta 0} + \hat{\phi}(\phi_i)H_{\phi 0}\right] e^{i\vec{k}_i\cdot\vec{r}}$$

where

$$\vec{k}_i = k\,\hat{n}_i, \quad \hat{\theta}(\theta_i,\phi_i) = \hat{\rho}(\phi_i)\cos\theta_i - \hat{x}_3\sin\theta_i, \quad \hat{\phi}(\phi_i) = -\hat{x}_1\sin\phi_i + \hat{x}_2\cos\phi_i$$

and $Z = \sqrt{\mu_0/\varepsilon_0} \cong 120\pi\,[\Omega]$ is the characteristic impedance of free space (see Fig 2). These 4 scalar field quantities are related by $H_{\theta 0} = E_{\phi 0}/Z$, $E_{\theta 0} = -Z\,H_{\phi 0}$. When one inserts $E_{\phi 0} = E_{\theta 0}e^{i\delta}$, the polarization of the incoming wave is also included in the formulation via an arbitrary phase delay δ.

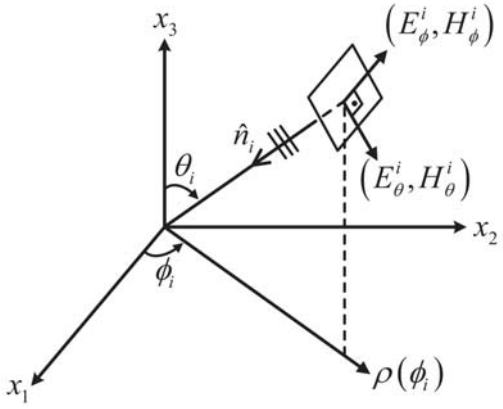

Figure 2. Plane wave incidence in an arbitrary direction.

2.1. The Physical Optics Currents on the Plate

In order to calculate the field reflected from the interface, we decompose the incident field into TE and TM components as in Fig. 3 in the semi-plane of incidence $O\rho(\theta_i)x_3$ as

$$\vec{E}^i_{TE} = \hat{\phi}(\phi_i)E_{\phi 0}\,e^{i\vec{k}_i\cdot\vec{r}}, \quad \vec{H}^i_{TE} = \frac{1}{Z}E_{\phi 0}\hat{\theta}(\theta_i,\phi_i)\,e^{i\vec{k}_i\cdot\vec{r}}$$
$$\vec{H}^i_{TM} = \hat{\phi}(\phi_i)H_{\phi 0}\,e^{i\vec{k}_i\cdot\vec{r}}, \quad \vec{E}^i_{TM} = -Z\,H_{\phi 0}\,\hat{\theta}(\theta_i,\phi_i)\,e^{i\vec{k}_i\cdot\vec{r}}$$

The boundary relations on the dielectric interface dictate that the reflected wave propagates in the direction $\hat{n}_r = \hat{r}(\theta_i,\pi+\phi_i) = \hat{\rho}(\pi+\phi_i)\sin\theta_i + \hat{x}_3\cos\theta_i$. Then, the reflected fields can be written as

$$\begin{cases} \vec{E}^r_{TE} = \hat{\phi}(\pi+\phi_i)R_{TE}E_{\phi 0}e^{i\vec{k}_r\cdot\vec{r}} \\ \vec{H}^r_{TE} = \frac{1}{Z}\hat{n}_r\times\vec{E}^r_{TE} = \dfrac{1}{Z}\hat{r}(\theta_i,\pi+\phi_i)\times\hat{\phi}(\pi+\phi_i)e^{i\vec{k}_r\cdot\vec{r}} = -\dfrac{1}{Z}R_{TE}E_{\phi 0}\hat{\theta}(\theta_i,\pi+\phi_i)\,e^{i\vec{k}_r\cdot\vec{r}} \end{cases}$$
$$\begin{cases} \vec{H}^r_{TM} = \hat{\phi}(\pi+\phi_i)R_{TM}H_{\phi 0}e^{i\vec{k}_r\cdot\vec{r}} \\ \vec{E}^r_{TM} = Z\,\vec{H}^r_{TM}\times\hat{n}_r = Z\,R_{TM}H_{\phi 0}\,\hat{\phi}(\pi+\phi_i)\times\hat{r}(\theta_i,\pi+\phi_i)\,e^{i\vec{k}_r\cdot\vec{r}} = Z\,R_{TM}H_{\phi 0}\,\hat{\theta}(\theta_i,\pi+\phi_i)\,e^{i\vec{k}_r\cdot\vec{r}} \end{cases}$$

with $\hat{\theta}(\theta_i,\pi+\phi_i) = \hat{\rho}(\pi+\phi_i)\cos\theta_i - \hat{x}_3\sin\theta_i$, $\vec{k}_r = k\,\hat{n}_r$ along with the Fresnel reflection coefficients

$$R_{TM} = \frac{N^2\cos\theta_i - \sqrt{N^2-\sin^2\theta_i}}{N^2\cos\theta_i + \sqrt{N^2-\sin^2\theta_i}}, \quad R_{TE} = \frac{\cos\theta_i - \sqrt{N^2-\sin^2\theta_i}}{\cos\theta_i + \sqrt{N^2-\sin^2\theta_i}}$$

The PO electric surface current density induced on the PEC plate is defined by

$$\vec{J}^{PO}_S = \hat{n}_S\times\left(\vec{H}^i + \vec{H}^r\right)\Big|_{x_1=0},\ x_2\in[-w/2,w/2],\ x_3\in[0,h].$$

The unit normal of the plate $\hat{n}_S$ is equal to $+\hat{x}_1$ or $-\hat{x}_1$ depending on the azimuthal angle of incidence being in the range $\phi_i\in[-\pi/2,\pi/2]$ or $\phi_i\in(\pi/2,\pi]\cup(-\pi,\pi/2)$. For the first choice, the PO currents read

$$\vec{J}^{PO}_S = \hat{n}_S\times\left(\vec{H}^i + \vec{H}^r\right)\Big|_{x_1=0} = \hat{x}_1\times\left(\vec{H}^i_{TE} + \vec{H}^i_{TM} + \vec{H}^r_{TE} + \vec{H}^r_{TM}\right)\Big|_{x_1=0} = \hat{x}_2J_{S2} + \hat{x}_3J_{S3}$$

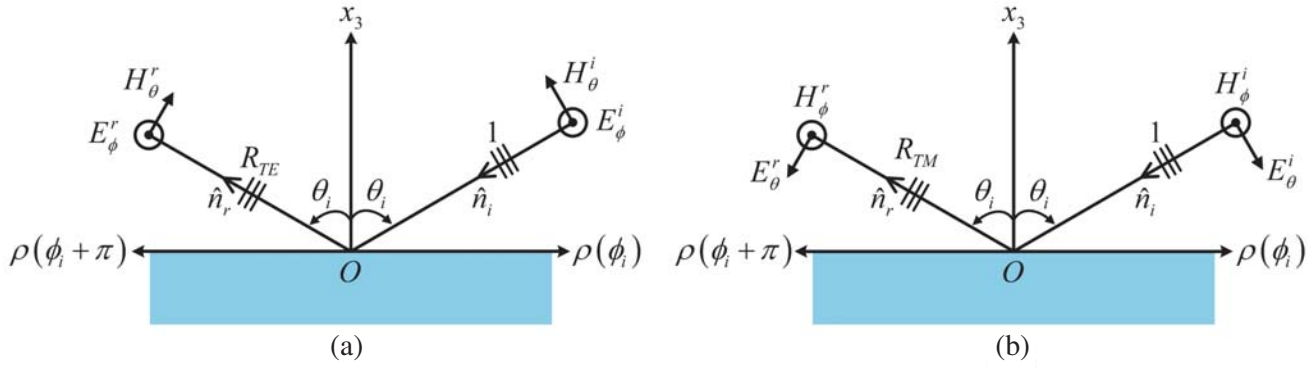

Figure 3. (a) TE and (b) TM decomposition of the incoming wave.

where

$$\begin{aligned} J_{S2}(x_2,x_3;\theta_i,\phi_i) &= \frac{1}{Z}E_{\phi 0}\sin\theta_i\left(e^{i\vec{k}_i\cdot\vec{r}}-R_{TE}e^{i\vec{k}_r\cdot\vec{r}}\right)\Big|_{x_1=0} \\ J_{S3}(x_2,x_3;\theta_i,\phi_i) &= \frac{1}{Z}E_{\phi 0}\cos\theta_i\sin\phi_i\left(e^{i\vec{k}_i\cdot\vec{r}}+R_{TE}e^{i\vec{k}_r\cdot\vec{r}}\right)\Big|_{x_1=0} \\ &\quad +H_{\phi 0}\cos\phi_i\left(e^{i\vec{k}_i\cdot\vec{r}}-R_{TM}e^{i\vec{k}_r\cdot\vec{r}}\right)\Big|_{x_1=0} \end{aligned}$$

with

$$\begin{aligned} \exp(i\vec{k}_i\cdot\vec{r})\Big|_{x_1=0} &= \exp\left[-ik\left(x_2\sin\theta_i\sin\phi_i+\ x_3\cos\theta_i\right)\right], \\ \exp(i\vec{k}_r\cdot\vec{r})\Big|_{x_1=0} &= \exp\left[-ik\left(x_2\sin\theta_i\sin\phi_i-\ x_3\cos\theta_i\right)\right]. \end{aligned}$$

2.2. The Components of the Green Dyadic

The FF-EFIE reveals the expression of the scattered PO electric field in air by the integral

$$\vec{E}^{PO}(\vec{r}) = i\omega\mu_0\int_S \bar{\bar{G}}(\vec{r},\vec{r}\,')\cdot\vec{J}_S^{PO}(\vec{r}\,')\,dS'$$

calculated over the PEC plate. Here, the Green dyadic has the general representation

$$\bar{\bar{G}} = \hat{x}_1\hat{x}_1g_1^1+\hat{x}_2\hat{x}_1g_2^1+\hat{x}_3\hat{x}_1g_3^1\ +\hat{x}_1\hat{x}_2g_1^2+\hat{x}_2\hat{x}_2g_2^2+\hat{x}_3\hat{x}_2g_3^2\ +\hat{x}_1\hat{x}_3g_1^3+\hat{x}_2\hat{x}_3g_2^3+\hat{x}_3\hat{x}_3g_3^3$$

where g_b^a stands for the total b-axis electrical field component generated at $\vec{r}=(x_1,x_2,x_3)$ by the Hertzian dipole (with unit moment) located at $\vec{r}\,'=(x_1',x_2',x_3')$ and directed along a-axis. The location of the plate in our present problem requires incorporating only 6 out of 9 dyads:

$$\bar{\bar{G}}\cdot\vec{J}_S^{PO}\Big|_{x_1=0} = \hat{x}_1\left(g_1^2J_{S2}+g_1^3J_{S3}\right)\big|_{x_1=0}+\hat{x}_2\left(g_2^2J_{S2}+g_2^3J_{S3}\right)\big|_{x_1=0}+\hat{x}_3\left(g_3^2J_{S2}+g_3^3J_{S3}\right)\big|_{x_1=0}$$

Then, we may define

$$\frac{e^{ikr}}{kr}\Delta_{bN}^{a(d,i,s)} \triangleq i\omega\mu_0\int_S g_b^{a(d,i,s)}J_{SN}\Big|_{x_1'=0}\,dS'$$

and the Cartesian components of the PO electric field can be written as

$$\vec{E}^{PO}(\vec{r}) = \hat{x}_1E_1+\hat{x}_2E_2+\hat{x}_3E_3$$

with

$$E_j = E_j^{(d)}+E_j^{(i)}+E_j^{(s)},\ \ j=1,2,3$$

where

$$E_1^{(d,i,s)} = \left[\Delta_{12}^{2(d,i,s)} + \Delta_{13}^{3(d,i,s)}\right]\frac{e^{ikr}}{kr},$$
$$E_2^{(d,i,s)} = \left[\Delta_{22}^{2(d,i,s)} + \Delta_{23}^{3(d,i,s)}\right]\frac{e^{ikr}}{kr},$$
$$E_3^{(d,i,s)} = \left[\Delta_{32}^{2(d,i,s)} + \Delta_{33}^{3(d,i,s)}\right]\frac{e^{ikr}}{kr}.$$

While the formulation has no restriction so far on the source frequency and the values of the constitutive parameters of the simple lossy dielectric half-space, we shall continue with the explicit representations of the Green functions delivered by King under High Contrast Approximation (HCA) $|N| \geq 3$ for the planar interface (cf. [11]). We shape the Green functions available in cylindrical coordinate representation in literature into Cartesian form. This is the same set of functions employed earlier by one of the authors [12] to investigate electromagnetic scattering from metallic thin wire structures located over a planar simple lossy dielectric half-space and are given for $x_3, x_3' \geq 0$ as follows:

$$\begin{aligned}
g_1^1 &= \frac{e^{ikR_1}}{4\pi R_1}\left[\xi_1 - \frac{(x_1-x_1')^2}{R_1^2}\xi_2\right] - \frac{e^{ikR_2}}{4\pi R_2}\left[\eta_1 - \frac{(x_1-x_1')^2}{R_2^2}\eta_2\right] \\
&\quad + \frac{e^{ikR_2}}{2\pi R_2}\frac{1}{N}\left\{\frac{(x_3+x_3')}{R_2}\eta_3 - \frac{\eta_1}{N} + \frac{(x_2-x_2')^2}{R_2^2}\frac{\eta_2}{N} - \frac{\Xi}{N^2}\frac{R_2}{P^3}\left[ikR_2(x_1-x_1')^2 + \frac{R_2^2}{P^2}(x_2-x_2')^2\right]\right\} \\
g_2^1 &= -\frac{(x_1-x_1')(x_2-x_2')}{R_1^2}\frac{e^{ikR_1}}{4\pi R_1}\xi_2 + \frac{(x_1-x_1')(x_2-x_2')}{R_2^2}\frac{e^{ikR_2}}{4\pi R_2}\eta_2 \\
&\quad - \frac{(x_1-x_1')(x_2-x_2')}{R_2^2}\frac{e^{ikR_2}}{2\pi R_2}\frac{\Xi}{N^2}\left[\eta_2 + \frac{1}{N}\frac{R_2^3}{P^3}\left(ikR_2 - \frac{R_2^2}{P^2}\right)\right] \\
g_3^1 &= -\frac{(x_1-x_1')(x_3-x_3')}{R_1^2}\frac{e^{ikR_1}}{4\pi R_1}\xi_2 + \frac{(x_1-x_1')(x_3+x_3')}{R_2^2}\frac{e^{ikR_2}}{4\pi R_2}\eta_2 - \frac{(x_1-x_1')}{R_2}\frac{e^{ikR_2}}{2\pi R_2}\frac{1}{N}\left[\eta_3 + \frac{\Xi}{N}ikR_2\frac{R_2}{P}\right] \\
g_1^2 &= -g_2^1 \\
g_2^2 &= \frac{e^{ikR_1}}{4\pi R_1}\left[\xi_1 - \frac{(x_2-x_2')^2}{R_1^2}\xi_2\right] - \frac{e^{ikR_2}}{4\pi R_2}\left[\eta_1 - \frac{(x_2-x_2')^2}{R_2^2}\eta_2\right] \\
&\quad + \frac{e^{ikR_2}}{2\pi R_2}\frac{1}{N}\left\{\frac{(x_3+x_3')}{R_2}\eta_3 - \frac{\eta_1}{N} + \frac{(x_1-x_1')^2}{R_2^2}\frac{\eta_2}{N} - \frac{\Xi}{N^2}\frac{R_2}{P^3}\left[ikR_2(x_2-x_2')^2 + \frac{R_2^2}{P^2}(x_1-x_1')^2\right]\right\} \\
g_3^2 &= -\frac{(x_2-x_2')(x_3-x_3')}{R_1^2}\frac{e^{ikR_1}}{4\pi R_1}\xi_2 + \frac{(x_2-x_2')(x_3+x_3')}{R_2^2}\frac{e^{ikR_2}}{4\pi R_2}\eta_2 - \frac{(x_2-x_2')}{R_2}\frac{e^{ikR_2}}{2\pi R_2}\frac{1}{N}\left[\eta_3 + \frac{\Xi}{N}ikR_2\frac{R_2}{P}\right] \\
g_1^3 &= -\frac{(x_1-x_1')(x_3-x_3')}{R_1^2}\frac{e^{ikR_1}}{4\pi R_1}\xi_2 - \frac{(x_1-x_1')(x_3+x_3')}{R_2^2}\frac{e^{ikR_2}}{4\pi R_2}\eta_2 + \frac{(x_1-x_1')}{R_2}\frac{e^{ikR_2}}{2\pi R_2}\frac{1}{N}\left[\eta_3 + \frac{\Xi}{N}ikR_2\frac{R_2}{P}\right] \\
g_2^3 &= -\frac{(x_2-x_2')(x_3-x_3')}{R_1^2}\frac{e^{ikR_1}}{4\pi R_1}\xi_2 - \frac{(x_2-x_2')(x_3+x_3')}{R_2^2}\frac{e^{ikR_2}}{4\pi R_2}\eta_2 + \frac{(x_2-x_2')}{R_2}\frac{e^{ikR_2}}{2\pi R_2}\frac{1}{N}\left[\eta_3 + \frac{\Xi}{N}ikR_2\frac{R_2}{P}\right] \\
g_3^3 &= \frac{e^{ikR_1}}{4\pi R_1}\left[\xi_1 - \frac{(x_3-x_3')^2}{R_1^2}\xi_2\right] + \frac{e^{ikR_2}}{4\pi R_2}\left[\eta_1 - \frac{(x_3+x_3')^2}{R_2^2}\eta_2\right] + \frac{\Xi}{N}ikP\frac{e^{ikR_2}}{2\pi R_2}
\end{aligned}$$

Here,

$$\begin{aligned}
R_{1,2} &= \left|\vec{r} \mp \vec{r}'\right| = \left[(x_1-x_1')^2 + (x_2-x_2')^2 + (x_3 \mp x_3')^2\right]^{1/2}, \\
P &= \left[(x_1-x_1')^2 + (x_2-x_2')^2\right]^{1/2} \\
\xi_1 &= 1 - 1/ikR_1 + 1/k^2R_1^2, \quad \xi_2 = 1 - 3/ikR_1 - 3/k^2R_1^2 \\
\eta_1 &= 1 - 1/ikR_2 + 1/k^2R_2^2, \quad \eta_2 = 1 - 3/ikR_2 - 3/k^2R_2^2, \quad \eta_3 = 1 - 1/ikR_2
\end{aligned}$$

$U = \frac{kR_2}{2N^2}[\frac{R_2+N(x_3+x_3')}{P}]^2$ is called *Sommerfeld numerical distance* and

$$\Xi = \sqrt{\frac{\pi}{kR_2}} e^{-iU} \left[\frac{1}{2}(1+i) - C_2(U) - iS_2(U)\right]$$

where

$$C_2(U) + iS_2(U) = \int_U^\infty \frac{\exp(it)}{\sqrt{2\pi t}} dt$$

is the complex Fresnel function. We may use the relation

$$e^{-iU} \left[\frac{1}{2}(1+i) - C_2(U) - iS_2(U)\right] = \frac{1}{2}(1+i)\, \varpi\left(e^{i\pi/4}\sqrt{U}\right)$$

to express Ξ in the compact form

$$\Xi = \frac{e^{i\pi/4}}{\sqrt{2}}\, \varpi\left(e^{i\pi/4}\sqrt{U}\right) \sqrt{\frac{\pi}{kR_2}}$$

in terms of the complex Faddeeva function (cf. [13], Ch. 7)

$$\varpi(z) = \exp\left(-z^2\right) \operatorname{erfc}\left(-iz\right), \quad z \in \mathrm{C}$$

The (Cartesian) Green dyadic and its each component constitute *direct*, *perfect image*, and *surface wave* components, which we shall notate as

$$\bar{\bar{G}} = \bar{\bar{G}}_d + \bar{\bar{G}}_i + \bar{\bar{G}}_s, \quad g_b^a = g_b^{a(d)} + g_b^{a(i)} + g_b^{a(s)}$$

The perfect image terms correspond to the reflected fields in presence of a PEC surface located on $x_3 = 0$ plane. The PEC boundary condition requires

$$\Delta_{12}^{2(d)} + \Delta_{12}^{2(i)} + \Delta_{13}^{3(d)} + \Delta_{13}^{3(i)}\Big|_{x_3=0} = 0$$
$$\Delta_{22}^{2(d)} + \Delta_{22}^{2(i)} + \Delta_{23}^{3(d)} + \Delta_{23}^{3(i)}\Big|_{x_3=0} = 0$$

and the surface wave components $\bar{\bar{G}}_s$ vanish in the limit $|N| \to \infty$. The feature of King's representation is the possibility to compare the scattered fields in presence of a simple lossy dielectric half-space with the results for the special case of a PEC ground by dropping the contributions due to $\bar{\bar{G}}_s$.

2.3. Far Field Approximations in the Green Dyadic

As we only require the calculation of the Green dyadic in the far field, the following substitutions in amplitude and phase terms are adequate before computation:

$(x_1 - x_1') \to x_1 = r\sin\theta\cos\phi, \quad (x_2 - x_2') \to x_2 = r\sin\theta\sin\phi, \quad (x_3 - x_3') \to x_3 = r\cos\theta$

$R_{1,2} \to r, \quad P \to \rho = r\sin\theta$

$\xi_1, \eta_1 \to 1 - 1/ikr - 1/k^2r^2, \quad \xi_2, \eta_2 \to 1 - 3/ikr - 3/k^2r^2$

$\exp(ikR_1) \to \exp(ikr)\exp(-ik\hat{r}\cdot\vec{r}\,'), \quad \exp(ikR_2) \to \exp(ikr)\exp(+ik\hat{r}\cdot\vec{r}\,')$

$\exp\left(\pm ik\hat{r}\cdot\vec{r}\,'\right) = \exp\left[\pm ik(x_2'\sin\theta\sin\phi + x_3'\cos\theta)\right]$

$$U \to \frac{kr}{2N^2}\left[\frac{r+N(x_3+x_3')}{\rho}\right]^2 = \frac{kr}{2N^2}\left(\frac{r}{\rho}\right)^2\left[1+\frac{N(x_3+x_3')}{r}\right]^2 = \frac{kr}{2N^2\sin^2\theta}\left[1+N\left(\cos\theta+\frac{x_3'}{r}\right)\right]^2$$

$$\Xi \to \frac{e^{i\pi/4}}{\sqrt{2}}\, \varpi\left(e^{i\pi/4}\sqrt{U}\right)\sqrt{\frac{\pi}{kr}}$$

x_3' in U remains as it is (along with $\cos\theta$) since $\cos\theta + x_3'/r$ may take values comparable to 1 when multiplied by N.

Explicit expressions of $\Delta_{bN}^{a(d,i,s)}$ are provided in Appendix. Right over the interface (as $\theta \to \pi/2$) one may observe the conditions

$$\Delta_{12}^{2(d+i)} = 0, \quad \Delta_{13}^{3(d+i)} = 0, \quad \Delta_{22}^{2(d+i)} = 0, \quad \Delta_{23}^{3(d+i)} = 0, \quad \Delta_{32}^{2(d)} = \Delta_{32}^{2(i)}, \quad \Delta_{33}^{3(d)} = \Delta_{33}^{3(i)}$$

which read

$$E_1^{(d+i)} = 0, \quad E_1 = E_1^{(s)}, \quad E_2^{(d+i)} = 0, \quad E_2 = E_2^{(s)}, \quad E_3^{(d+i)} = 2\left[\Delta_{32}^{2(d)} + \Delta_{33}^{3(d)}\right] \frac{e^{ikr}}{kr}$$

in accord with the boundary conditions that the tangential electric field components (of the space wave) vanish while the normal component maximizes on a PEC surface.

3. A PROCEDURE TO CALCULATE FREE SPACE RCS OF TARGETS LOCATED OVER A TRANSMISSIVE HALF-SPACE

The conventional microwave RCS of a target in free space (RCS^{fs}) is defined by

$$RCS^{fs}\left(\theta_R, \varphi_R; \theta_T, \varphi_T; f\right) = \lim_{r_{RS}\to\infty} 4\pi r_{RS}^2 \frac{\bar{P}_{RS}^{fs}}{\bar{P}_{ST}^{fs}} = \lim_{r_{RS}\to\infty} 4\pi r_{RS}^2 \frac{\left|\vec{E}_{RS}^{fs}\right|^2}{\left|\vec{E}_{ST}^{fs}\right|^2} \tag{1}$$

with

$$\begin{aligned}
\vec{H}_{RS}^{fs} &= \frac{1}{Z}\hat{r}_{RS} \times \vec{E}_{RS}^{fs}, \quad \vec{H}_{ST}^{fs} = \frac{1}{Z}\hat{r}_{ST} \times \vec{E}_{ST}^{fs} \\
\bar{P}_{RS}^{fs} &= \hat{r}_{RS} \cdot \Re\left\{\frac{1}{2}\vec{E}_{RS}^{fs} \times \vec{H}_{RS}^{fs*}\right\} \simeq \frac{1}{2Z}\left|\vec{E}_{RS}^{fs} \cdot \hat{l}_R\right|^2 \cong \frac{P_{RS}^{fs}(\theta_R, \varphi_R; f)}{4\pi r_{RS}^2} \\
\bar{P}_{ST}^{fs} &= \hat{r}_{ST} \cdot \Re\left\{\frac{1}{2}\vec{E}_{ST}^{fs} \times \vec{H}_{ST}^{fs*}\right\} = \frac{1}{2Z}\left|\vec{E}_{ST}^{fs} \cdot \hat{l}_S\right|^2
\end{aligned}$$

for $kr_{RS} \gg 1$, where $(r_T, \theta_T, \varphi_T)$ and $(r_R, \theta_R, \varphi_R)$ denote the spherical coordinates of the transmitter and receiver antennas; $r_{RS} = |\vec{r}_{RS}| = |\vec{r}_R - \vec{r}_S|$; $(\vec{E}_{RS}^{fs}, \vec{H}_{RS}^{fs})$ are the scattered fields at the receiver, and $(\vec{E}_{ST}^{fs}, \vec{H}_{ST}^{fs})$ are the fields incident on the target (see Fig. 4).

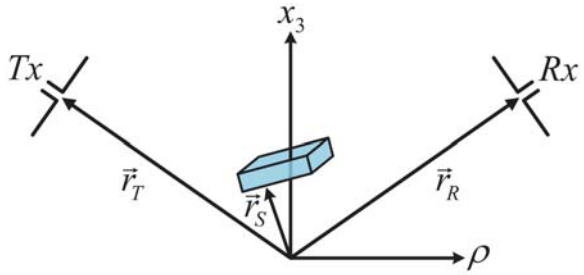

Figure 4. Bistatic RCS set-up in free space.

In this definition, it is assumed that the transmitter is located at infinity, i.e., a homogeneous plane wave incidence is considered, and $r_{ST} = |\vec{r}_{ST}| = |\vec{r}_S - \vec{r}_T|$ is not involved. The limiting process guarantees RCS^{fs} to be range independent. We also assume that the target and the receiver are oriented along the dummy directions $\hat{l}_S$ and $\hat{l}_R$ for full reception so that one can easily relate the closed form RCS pattern to the individual patterns of the field components involved.

RCS^{fs} has 3 essential features:

(i) it has dimension of $[\mathrm{m}]^2$,

(ii) it is range independent,

(iii) it is a measure of the ratio of the scattered power density from the target in the direction of the receiver to the power density that is intercepted by the target.

In case when the sources are located at a finite distance from the target (cf. [14]), and/or lower frequency bands are concerned, and/or the medium is non-simple, the scattered fields may have arbitrary asymptotic behaviors due to the impacts of operating frequency, locations of transmitter/target/receiver and geometrical and physical properties of the ambient medium. For such scenarios, including our present problem where certain portion of total power is transmitted by surface waves, we introduce a unitless *correction factor* $C(r_{ST}, r_{RS})$ defined by

$$RCS^{fs}\left(\theta_R, \varphi_R; \theta_T, \varphi_T; f\right) \triangleq \lim_{r_{ST}, r_{RS} \to \infty} 4\pi r_{RS}^2 C(r_{ST}, r_{RS}) \frac{\bar{P}_{RS}}{\bar{P}_{ST}} \tag{2}$$

where

$$\bar{P}_{RS} = \hat{r}_{RS} \cdot \Re\left\{\frac{1}{2}\vec{E}_{RS} \times \vec{H}_{RS}^*\right\}, \quad \bar{P}_{ST} = \hat{r}_{ST} \cdot \Re\left\{\frac{1}{2}\vec{E}_{ST} \times \vec{H}_{ST}^*\right\}.$$

We assert that such a calibration shall serve to reach at RCS^{fs} approximately over measured/calculated values of $\bar{P}_{RS}$ and $\bar{P}_{ST}$, which are governed by the geometrical and physical properties of the medium under consideration, as follows:

(i) Measure/Calculate $\bar{P}_{ST}$ and $\bar{P}_{RS}$ in the far field for a specific scenario.

(ii) Calculate $4\pi r_{RS}^2 C(r_{ST}, r_{RS})\bar{P}_{RS}/\bar{P}_{ST}$ by using the predetermined value of $C(r_{ST}, r_{RS})$ in the given range.

We are particularly interested in the special case when the target and the receiver are located very close to the (planar or spherical) ground. In this case the Norton representations of electromagnetic fields on a dielectric half-space serve better to our purpose (see [15, 16]), where the total scattered fields $(\vec{E}_{RS}, \vec{H}_{RS})$ over the ground can be related to the free space fields $(\vec{E}_{RS}^{fs}, \vec{H}_{RS}^{fs})$ approximately by

$$\hat{\theta}\left(\hat{\theta} \cdot \vec{E}_{RS}\right) \cong 2\vec{E}_{RS}^{fs} F_{RS}\Big|_{x_3=0} \tag{3a}$$

$$\vec{H}_{RS} \cong 2\vec{H}_{RS}^{fs} F_{RS}\Big|_{x_3=0} \tag{3b}$$

$$\vec{H}_{RS} \cong \frac{1}{Z}\hat{r}_{RS} \times \vec{E}_{RS}\Big|_{x_3=0} \tag{3c}$$

with

$$\bar{P}_{RS} \cong \frac{1}{2Z}\left|\vec{E}_{RS}\right|^2 \cong \frac{1}{2Z}\left|\vec{E}_{RS}^{fs}\right|^2 4\left|F_{RS}\right|^2\Big|_{x_3=0} \tag{3d}$$

with

$$F_{RS} = 1 + i\sqrt{\pi U_{RS}}\varpi(\sqrt{U_{RS}}) \tag{3e}$$

representing the Norton attenuation factor.

There are two critical distances that determine the asymptotic behavior of the fields radiated over ground: $\rho_C = a(ka/2)^{-1/3}$ is the critical distance [17] after which the diffraction effects due to earth's sphericity cannot be disregarded; and $\rho_i = 8|N|^2/k$. Here, $a = 6378$ [km] represents earth's radius. The asymptotic behaviors of the scattered fields depending on ρ_C and ρ_i are illustrated in Figs. 5 and 6 following [17] and [18].

3.1. The Special Case of Homogeneous Plane Wave Incidence

In this case, the power density directed at the target is calculated by

$$\begin{aligned}\bar{P}_{ST} &= \hat{r}_{ST} \cdot \Re\left\{\frac{1}{2}\vec{E}_{ST} \times \vec{H}_{ST}^*\right\} \\ &= \frac{1}{2}\hat{r}_{ST} \cdot \Re\left\{\left(\vec{E}_{TE}^i + \vec{E}_{TE}^r\right) \times \left(\vec{H}_{TE}^i + \vec{H}_{TE}^r\right)^* + \left(\vec{E}_{TM}^i + \vec{E}_{TM}^r\right) \times \left(\vec{H}_{TM}^i + \vec{H}_{TM}^r\right)^*\right\}\end{aligned}$$

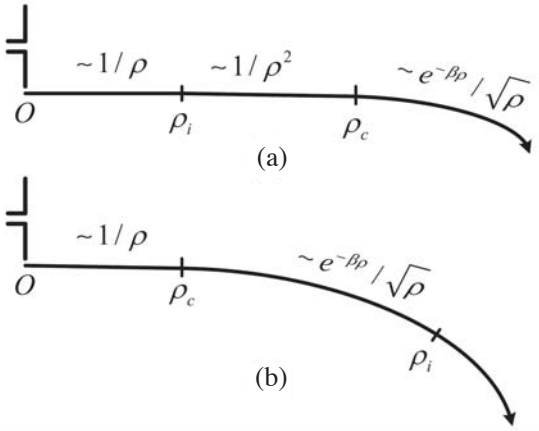

Figure 5. Asymptotic behavior of radiated fields over spherical earth for (a) $\rho_C \gg \rho_i$, (b) $\rho_C \ll \rho_i$.

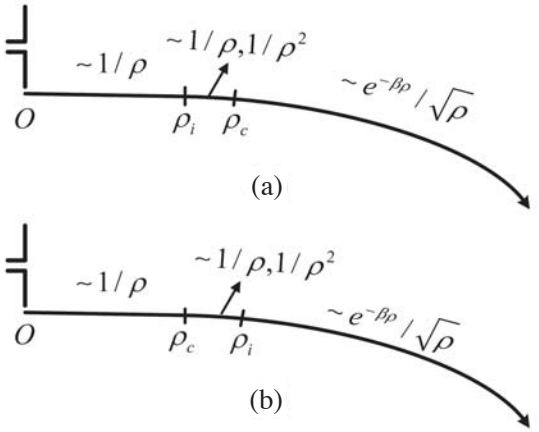

Figure 6. Asymptotic behavior of radiated fields over spherical earth for (a)$\rho_C \approx \rho_i$ with $\rho_C > \rho_i$ (b) $\rho_C \approx \rho_i$ with $\rho_C < \rho_i$.

When we pick origin as the reference point for calculation of total power density, the individual terms are calculated as

$$\left(\vec{E}^i_{TE} + \vec{E}^r_{TE}\right) \times \left(\vec{H}^i_{TE} + \vec{H}^r_{TE}\right)^* = \frac{1}{Z} |E_{\phi 0}|^2 (R_{TE} - 1) \times (\hat{r}(\theta_i, \phi_i) + R^*_{TE} \hat{r}(\theta_i, \pi + \phi_i))$$
$$\left(\vec{E}^i_{TM} + \vec{E}^r_{TM}\right) \times \left(\vec{H}^i_{TM} + \vec{H}^r_{TM}\right)^* = Z |H_{\phi 0}|^2 (R^*_{TM} - 1) \times (\hat{r}(\theta_i, \phi_i) + R_{TM} \hat{r}(\theta_i, \pi + \phi_i))$$

This reveals

$$\vec{E}_{ST} \times \vec{H}^*_{ST} = D\hat{r}(\theta_i, \phi_i) + E\hat{r}(\theta_i, \pi + \phi_i) \tag{4a}$$
$$D \triangleq \frac{1}{Z} |E_{\phi 0}|^2 (R_{TE} - 1) + Z |H_{\phi 0}|^2 (R^*_{TM} - 1) \tag{4b}$$
$$E \triangleq \frac{1}{Z} |E_{\phi 0}|^2 (R_{TE} - 1) R^*_{TE} + Z |H_{\phi 0}|^2 (1 - R^*_{TM}) R_{TM} \tag{4c}$$

By definition, the target is assumed to be directed in a hypothetical direction that collects the entire incoming power flux. This requires expressing the incoming power density as

$$\bar{P}_{ST} = \frac{1}{2} \left| \vec{E}_{ST} \times \vec{H}^*_{ST} \right| = \frac{1}{2} \sqrt{\sin^2 \theta_i |D - E|^2 + \cos^2 \theta_i |D + E|^2} \tag{5a}$$

This shapes Eq. (2) into

$$\begin{aligned} RCS^{fs}(\theta_R,\varphi_R;\theta_T,\varphi_T;f) &= \lim_{r_{RS}\to\infty} 4\pi r_{RS}^2 C(r_{RS})\frac{\bar{P}_{RS}}{\bar{P}_{ST}} \\ &\cong \lim_{r_{RS}\to\infty} 4\pi r_{RS}^2 C(r_{RS})\frac{1}{\bar{P}_{ST}}\frac{1}{2Z}\left|\vec{E}_{RS}^{fs}\right|^2 4\left|F_{RS}\right|^2\Big|_{x_3=0} \\ &= \lim_{r_{RS}\to\infty} 4\pi r_{RS}^2 C(r_{RS})\frac{1}{\bar{P}_{ST}}\frac{(1/2Z)\left|\vec{E}_{RS}^{fs}\right|^2}{(1/2Z)\left|\vec{E}_{ST}^{fs}\right|^2}\frac{1}{2Z}\left|\vec{E}_{ST}^{fs}\right|^2 4\left|\vec{F}_{RS}\right|^2\Big|_{x_3=0} \\ &= \lim_{r_{RS}\to\infty} 4\pi r_{RS}^2 C(r_{RS})4\left|\vec{F}_{RS}\right|^2\Big|_{x_3=0}\frac{1}{\bar{P}_{ST}}\frac{1}{2Z}\left|\vec{E}_{TE}^{i}+\vec{E}_{TM}^{i}\right|^2 RCS^{fs} \end{aligned}$$

so that $C(r_{RS})$ is specified by the condition

$$\lim_{r_{RS}\to\infty} 4\pi r_{RS}^2 C(r_{RS})4\left|F_{RS}\right|^2\Big|_{x_3=0}\frac{1}{\bar{P}_{ST}}\frac{1}{2Z}\left|\vec{E}_{TE}^{i}+\vec{E}_{TM}^{i}\right|^2 = 1,$$

i.e.,

$$C(r_{RS}) = \frac{1}{\bar{P}_{ST}}\frac{\left|\vec{E}_{TE}^{i}+\vec{E}_{TM}^{i}\right|^2\Big/2Z}{\lim_{r_{RS}\to\infty} 4\pi r_{RS}^2 4\left|F_{RS}\right|^2\Big|_{x_3=0}} = \frac{1}{\bar{P}_{ST}}\frac{\left(\left|E_{\phi 0}\right|^2+Z^2\left|H_{\phi 0}\right|^2\right)\Big/2Z}{\lim_{r_{RS}\to\infty} 4\pi r_{RS}^2 4\left|F_{RS}\right|^2\Big|_{x_3=0}} \tag{5b}$$

In the planar range we may consider the asymptotic behavior

$$F_{RS}\sim -\frac{1}{2U}+O(U^{-2}),\quad U\to\infty \ \text{ with } \ U=\frac{k\,r_{RS}}{2N^2}$$

when both the target and the receiver are located *on the ground*. This reveals

$$C\left(\theta_i,N;\theta=\pi/2\right) = \frac{1}{\bar{P}_{ST}}\frac{k^2\left(\left|E_{\phi 0}\right|^2+Z^2\left|H_{\phi 0}\right|^2\right)\Big/2Z}{16\pi|N|^4} \tag{6}$$

3.2. The Special Case of Ground Based Transmitter

In this case, we have the same form of equations as Eq. (3) between the transmitter and the scatterer:

$$\hat{\theta}\left(\hat{\theta}\cdot\vec{E}_{ST}\right)\cong 2\vec{E}_{ST}^{fs}F_{ST}\Big|_{x_3=0},\quad \vec{H}_{ST}\cong 2\vec{H}_{ST}^{fs}F_{ST}\Big|_{x_3=0}$$

$$\vec{H}_{ST}\cong\frac{1}{Z}\hat{r}_{ST}\times\vec{E}_{ST}\Big|_{x_3=0},\quad \bar{P}_{ST}\cong\frac{1}{2Z}\left|\vec{E}_{ST}^{fs}\right|^2 4\left|F_{ST}\right|^2\Big|_{x_3=0}$$

and Eq. (4b) is replaced by the condition

$$\lim_{r_{ST},r_{RS}\to\infty} 4\pi r_{RS}^2 C(r_{ST},r_{RS})\frac{\left|F_{RS}\right|^2}{\left|F_{ST}\right|^2} = 1,$$

which reveals

$$C(r_{ST},r_{RS}) = \frac{1}{4\pi\, r_{ST}\, r_{RS}}. \tag{7}$$

As range information is obtained separately in radar systems, the correction factor can be specified and employed coherently to reveal RCS^{fs} of the target. The computed RCS^{fs} may also be placed into the ground wave radar equations (cf. [19]) as

$$P_R = \frac{P_T\cdot G_T'\cdot G_R'\cdot(\lambda^2/4\pi)\cdot RCS^{fs}\cdot 4\cdot\left|F_{ST}\right|^2 4\cdot\left|F_{RS}\right|^2}{(4\pi r_{ST}^2)\cdot(4\pi r_{RS}^2)}$$

where P_T [W] is the transmitter has an output power; $G_{T,R}$ are free space antenna gains; $G_{T,R}'$ are the gains when the ground underneath the transmitter is screened by a PEC surface.

4. EVALUATION OF $I(\beta)$

Regarding the contribution of surface wave components in FF-EFIE, we require to compute integrals in the form

$$I(\beta) = I\left(\beta; kr, kh, \theta, N\right) \triangleq \int_0^{kh} \exp\left(i\beta\bar{x}_3'\right) \varpi\left(e^{i\pi/4}\sqrt{U}\right) d\bar{x}_3' \tag{8a}$$

where

$$\sqrt{U} = \sqrt{\frac{kr}{2}} \frac{1}{\sin\theta} \left[\frac{1}{N} + \cos\theta + \frac{\bar{x}_3'}{kr}\right] \in \mathbb{C}, \tag{8b}$$

$\bar{x}_3' = kx_3'$, $\theta \in [0, \pi/2)$, $\beta \in (-2, 2)$, $kr, kh > 0$. $|\sqrt{U}|$ is lower bounded by $U_{\min}$ as

$$\left|\sqrt{U}\right| \geq \sqrt{\frac{kr}{2}} \left|\frac{1}{N} + \frac{\bar{x}_3'}{kr}\right| \geq \frac{1}{|N|}\sqrt{\frac{kr}{2}}, \bar{x}_3' \in [0, kh].$$

The integral applies under the approximations $kr \gg 1$, $kh \gg 1$ and $|N| \geq 3$. Assuming that the constitutive parameters of the simple lossy half-space remain constant through HF-MW bands, the refractivity decreases smoothly with frequency.

Table 1. Variation of $|N|$ for different types of ground.

Medium	ε_r	$\sigma_{\mathrm{mS/m}}$	$\lvert N\rvert$ at $f_{\mathrm{MHz}} = 3$	$\lvert N\rvert$ at $f_{\mathrm{GHz}} = 30$
Sea water	80	4000	154.92	8.95
Wet earth	12	400	48.99	3.46
Dry earth	8	40	15.50	2.83
Lake water	80	4	9.14	8.94

In Table 1, we outline the values of $|N|$ at the two ends of our spectrum under consideration. For the given parametric range we have

$$\begin{aligned}
&\Re\{N\} > \Im\{N\} \geq 0, \quad \angle N \in [0, \pi/4) \\
\Re\left\{\sqrt{U}\right\} &= \sqrt{\frac{kr}{2}} \frac{1}{\sin\theta} \left[\frac{\Re\{N\}}{|N|^2} + \cos\theta + \frac{\bar{x}_3'}{kr}\right] > 0, \quad \Im\left\{\sqrt{U}\right\} = -\sqrt{\frac{kr}{2}} \frac{1}{\sin\theta} \frac{\Im\{N\}}{|N|^2} \leq 0, \\
\angle\sqrt{U} &= -\tan^{-1}\left(\frac{\Im\{N\}}{\Re\{N\} + |N|^2\left(\cos\theta + \bar{x}_3'/kr\right)}\right) \in (-\pi/4, 0], \quad \angle e^{i\pi/4}\sqrt{U} \in (0, \pi/4]
\end{aligned}$$

and therefore, $\Re\{e^{i\pi/4}\sqrt{U}(\bar{x}_3')\} > 0$, $\Im\{e^{i\pi/4}\sqrt{U}(\bar{x}_3')\} > 0$.

The smooth decay/variation of the magnitude/phase of the attenuation function $\varpi(e^{i\pi/4}\sqrt{U})$ in the vertical direction in Figs. 7, 8 reveal that the numerical integration of Eq. (8a) converges very rapidly. This can be managed by either some recursive adaptive quadrature of a popular programming language (such as "integral" command of MATLAB^{TM}) or as a simple Riemannian integral

$$I(\beta) \cong \sum_{j=1}^{\bar{h}\cdot M} \Delta x \cdot A(x_j) \exp\left(i\beta x_j\right)$$

where

$$\bar{h} = h/\lambda, \;\; \Delta x = k\lambda/M = 2\pi/M, \;\; kh = \bar{h}\cdot M\cdot\Delta x, \;\; x_j = \Delta x(j - 1/2), \;\; j = 1, \ldots, \bar{h}\cdot M; \;\; \bar{h}, M \in \mathbb{Z}^+$$

$$A(x_j) = \varpi\left(e^{i\pi/4}\sqrt{U_j}\right), \;\; \sqrt{U_j} = \sqrt{\frac{kr}{2}} \frac{1}{\sin\theta} \left[\frac{1}{N} + \cos\theta + \frac{x_j}{kr}\right]$$

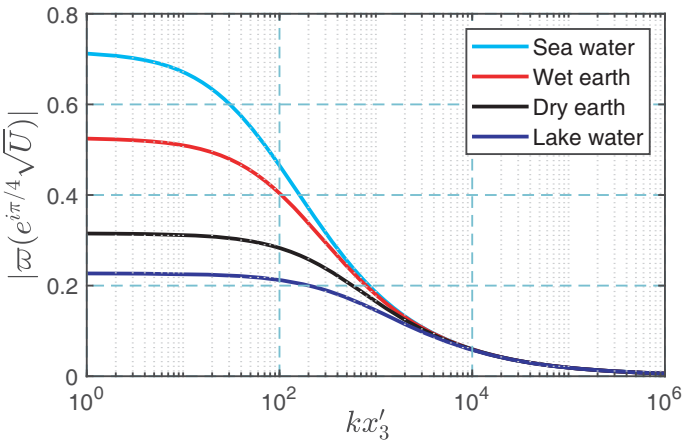

Figure 7. Variation of $|\varpi(e^{i\pi/4}\sqrt{U})|$ with kx_3' for $f_{\text{MHz}} = 3$, $r = 1000\lambda$.

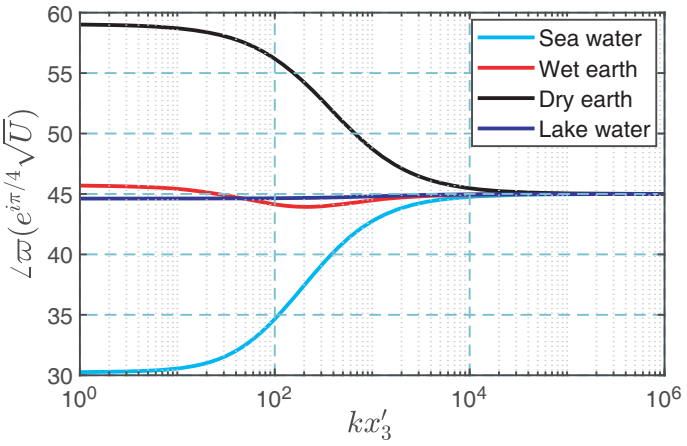

Figure 8. Variation of $\angle\varpi(e^{i\pi/4}\sqrt{U})$ with kx_3' for $f_{\text{MHz}} = 3$, $r = 1000\lambda$.

with $\min(M) = 30$ for sufficient accuracy. In computations we use Faddeeva.m file written by Abrarov and Quine in [20], which works with accuracy over 1e-13 in entire complex plane. Figs. 7, 8 comply with the asymptotic behaviors of the Faddeeva function [21]

$$\varpi(z) \sim \exp(-z^2)\left(1 + \frac{2i}{\sqrt{\pi}}\sum_{n=0}^{\infty}\frac{z^{2n+1}}{n!(2n+1)}\right), \quad |z| \ll 1$$

$$\varpi(z) \sim \frac{i}{\sqrt{\pi}}\frac{\exp(-2z^2)}{z}\left(1 - \sum_{n=1}^{\infty}\frac{(2n-1)!!}{(2z^2)^n}\right), \quad \Im\{z\} \geq 10$$

5. COMPUTATION OF SCATTERED ELECTRIC FIELDS

The scattered θ- and ϕ- components of the total electric field can be synthesized in terms of Cartesian components as

$$\begin{aligned} E_\theta^{PO} &= \hat{\theta}\cdot(\hat{x}_1E_1 + \hat{x}_2E_2 + \hat{x}_3E_3) = \cos\theta\cos\phi E_1 + \cos\theta\sin\phi E_2 - \sin\theta E_3 \\ &= E_\theta^{PO(d+i)} + E_\theta^{PO(s)} \end{aligned}$$

$$E_\theta^{PO(d+i)} = \frac{e^{ikr}}{kr}\begin{bmatrix} \cos\theta\cos\phi\left(\Delta_{12}^{2(d)}+\Delta_{13}^{3(d)}+\Delta_{12}^{2(i)}+\Delta_{13}^{3(i)}\right) \\ +\cos\theta\sin\phi\left(\Delta_{22}^{2(d)}+\Delta_{23}^{3(d)}+\Delta_{22}^{2(i)}+\Delta_{23}^{3(i)}\right) \\ -\sin\theta\left(\Delta_{32}^{2(d)}+\Delta_{33}^{3(d)}+\Delta_{32}^{2(i)}+\Delta_{33}^{3(i)}\right) \end{bmatrix}$$

$$E_\theta^{PO(s)} = \frac{e^{ikr}}{kr}\left[\cos\theta\cos\phi\left(\Delta_{12}^{2(s)}+\Delta_{13}^{3(s)}\right)+\cos\theta\sin\phi\left(\Delta_{22}^{2(s)}+\Delta_{23}^{3(s)}\right)-\sin\theta\left(\Delta_{32}^{2(s)}+\Delta_{33}^{3(s)}\right)\right]$$

and

$$\begin{aligned} E_\phi^{PO} &= \hat{\phi}\cdot(\hat{x}_1E_1+\hat{x}_2E_2+\hat{x}_3E_3) = -\sin\phi E_1+\cos\phi E_2 \\ &= E_\phi^{PO(d+i)}+E_\phi^{PO(s)} \end{aligned}$$

with

$$E_\phi^{PO(d+i)} = \frac{e^{ikr}}{kr}\left[-\sin\phi\left(\Delta_{12}^{2(d)}+\Delta_{13}^{3(d)}+\Delta_{12}^{2(i)}+\Delta_{13}^{3(i)}\right)+\cos\phi\left(\Delta_{22}^{2(d)}+\Delta_{23}^{3(d)}+\Delta_{22}^{2(i)}+\Delta_{23}^{3(i)}\right)\right]$$

$$E_\phi^{PO(s)} = \frac{e^{ikr}}{kr}\left[-\sin\phi\left(\Delta_{12}^{2(s)}+\Delta_{13}^{3(s)}\right)+\cos\phi\left(\Delta_{22}^{2(s)}+\Delta_{23}^{3(s)}\right)\right]$$

Decibel values are defined by

$$E_{\theta,\phi}^{PO}[\text{dB}] = 20\log_{10}\left|E_{\theta,\phi}^{PO(d+i+s)}\right|, \quad E_{\theta,\phi}^{PO(s)}[\text{dB}] = 20\log_{10}\left|E_{\theta,\phi}^{PO(s)}\right|.$$

Right over the ground (as $\theta\to\pi/2$) the boundary conditions dictate

$$\Delta_{12}^{2(d+i)},\Delta_{13}^{3(d+i)},\Delta_{22}^{2(d+i)},\Delta_{23}^{3(d+i)},\Delta_{32}^{2(d+i)}\to 0$$

while $\Delta_{33}^{3(d+i)}$ maximizes. This reveals

$$E_\theta^{PO(d+i)}\Big|_{\theta=\frac{\pi}{2}} = -\frac{e^{ikr}}{kr}\Delta_{33}^{3(d+i)}E_\theta^{PO(s)} = -\frac{e^{ikr}}{kr}\left(\Delta_{32}^{2(s)}+\Delta_{33}^{3(s)}\right) \tag{9a}$$

$$E_\phi^{PO}\big|_{\theta=\frac{\pi}{2}} = \frac{e^{ikr}}{kr}\left[-\sin\phi\left(\Delta_{12}^{2(s)}+\Delta_{13}^{3(s)}\right)+\cos\phi\left(\Delta_{22}^{2(s)}+\Delta_{23}^{3(s)}\right)\right] \tag{9b}$$

We are particularly interested in comparisons of the radiated electric fields over simple lossy dielectric half-space and PEC ground as $\theta\to\pi/2$. Over PEC ground we set $R_{TE}=-1,\ R_{TM}=1$ in Eq. (9) and obtain

$$\begin{aligned} E_{PEC}^{PO}\big|_{\theta=\frac{\pi}{2}} &= E_\theta^{PO(d+i)}\Big|_{\theta=\pi/2,\ R_{TE}=-1,\ R_{TM}=1} \qquad (10a) \\ &= -i4\pi\,\bar{h}\bar{w}\xi_1\frac{e^{ikr}}{kr}\text{sinc}\left(\bar{w}A\right)\text{sinc}\left(\bar{h}B\right)\cos(\pi\bar{h}B)\left(E_{\phi0}\cos\theta_i\sin\phi_i+ZH_{\phi0}\cos\phi_i\right) \\ E_\phi^{PO(d+i)}\Big|_{\theta=\pi/2,\ R_{TE}=-1,\ R_{TM}=1} &= 0 \qquad (10b) \end{aligned}$$

When the target and Rx are located very close to the ground (as $\theta\to\pi/2$), the scattered magnetic fields behave like

$$\vec{H}^{PO}\cong\frac{1}{Z}\hat{r}\times\vec{E}^{PO} = \frac{1}{Z}\hat{r}\times\left(\hat{\theta}E_\theta^{PO}+\hat{\phi}E_\phi^{PO}\right)$$

with complex Poynting vector

$$\vec{P}_C^{PO} = \Re\left\{\frac{1}{2}\vec{E}^{PO}\times\vec{H}^{PO*}\right\}\cong\frac{1}{2Z}\hat{r}\left|E_\theta^{PO}\right|^2 = \hat{r}\bar{P}_{RS}.$$

The free-space RCS of the target can be extracted from the equation

$$RCS^{fs}(\theta_R=\pi/2,\varphi_R;\theta_T,\varphi_T;f)\cong 4\pi r_{RS}^2C(r_{RS})\frac{1}{\bar{P}_{ST}}\frac{\left|E_\theta^{PO}\right|^2}{2Z}$$

by substituting $\bar{P}_{ST}$ in Eq. (5a) and $C(r_{RS})$ in Eq. (6) to get

$$RCS^{fs}(\theta=\pi/2,\varphi;\theta_i,\varphi_i;f) \cong \frac{1}{\left(\sin^2\theta_i\,|D+E|^2+\cos^2\theta_i\,|-D+E|^2\right)} \times\frac{\left(|E_{\phi 0}|^2+Z^2\,|H_{\phi 0}|^2\right)}{8Z^2\,|N|^4}\left|\Delta_{33}^{3(d+i)}+\Delta_{32}^{2(s)}+\Delta_{33}^{3(s)}\right|^2_{\theta_R=\pi/2} \tag{11}$$

In numerical illustrations, we set $\bar{w}=w/\lambda=20$, $\bar{h}=h/\lambda=10$, $\theta=\pi/2$, $\theta_i=\pi/4$, $E_{\phi 0}=1$, $H_{\phi 0}=1$. In Fig. 9, the variation of the amplitude of the surface PO current density induced on the plate is observed as a standing wave pattern for $\phi_i=0$, $\phi=0$ and at $f_{\text{MHz}}=3$, where the ground is lake water. Insufficiency of PO approximation in satisfying the edge conditions constitutes the main deficiency of the formulation.

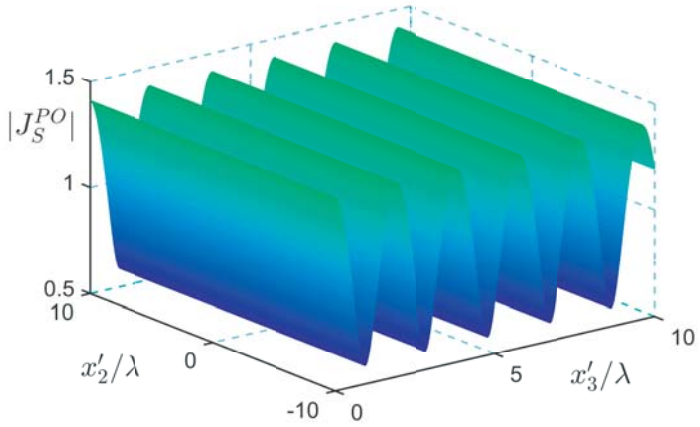

Figure 9. Variation of the amplitude of total surface current density $|\vec{J}_S^{PO}|$ over the plate.

In Figs. 10 and 11, the variations of θ- and ϕ-components of the total electric field are illustrated for $\phi_i=0$, $\phi=0$ at $f_{\text{MHz}}=3$. It is observed that the values of $|E_\theta|$ on the ground increase gradually proportional to $|N|$ in Table 1 and maximizes for PEC ground. The case is opposite for $|E_\phi|$ with much less values as dictated by the boundary conditions.

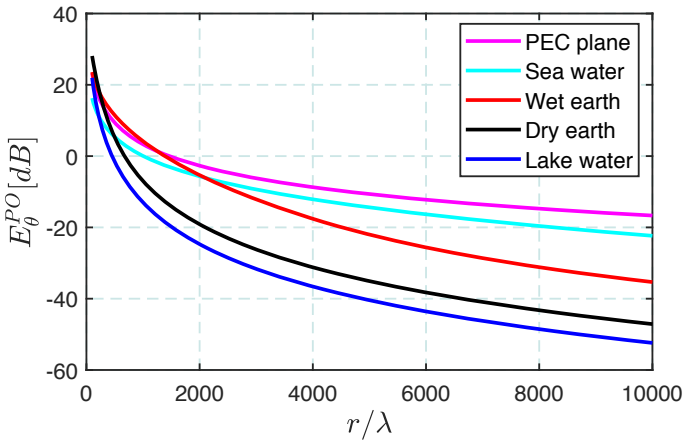

Figure 10. E_θ^{PO} [dB] for $r/\lambda\in(10^2,10^4)$ and $\theta=\pi/2$ at $f_{\text{MHz}}=3$.

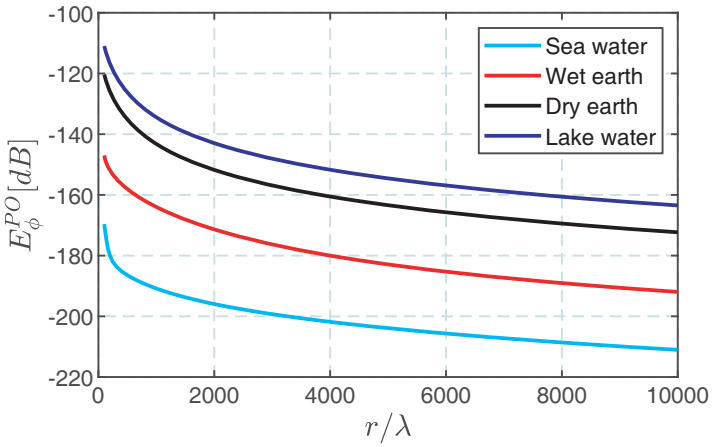

Figure 11. E_ϕ^{PO} [dB] for $r/\lambda \in (10^2, 10^4)$ and $\theta = \pi/2$ at $f_{\text{MHz}} = 3$.

One may observe from Figs. 10 and 11 that the values of tangential electric fields on a PEC surface and a simple lossy dielectric half-space are much different at $f_{\text{MHz}} = 3$ for a replacement. As illustrated in Figs. 12–14, this is actually the case in higher frequencies as well with an expanding gap.

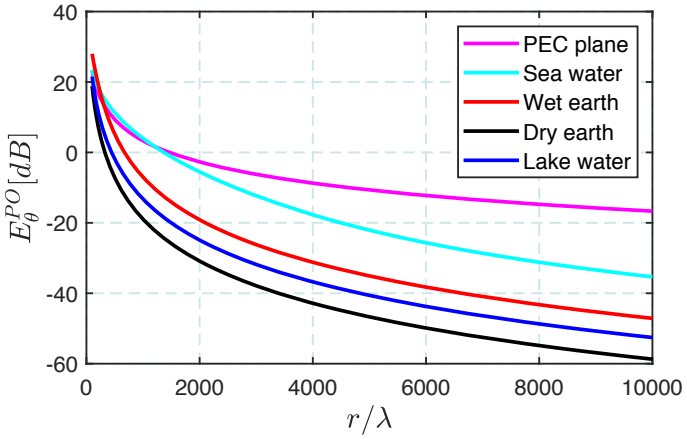

Figure 12. E_θ^{PO} [dB] for $r/\lambda \in (10^2, 10^4)$ and $\theta = \pi/2$ at $f_{\text{MHz}} = 30$.

The variations of the values of the integrals $I(B)$ and $I(C)$ in $\Delta_{bN}^{a(s)}$ outlined in Appendix are crucial for describing the parametric dependence and the stability of magnitude of surface wave components in the far field. These are depicted in Figs. 15–18 at $f_{\text{MHz}} = 3$, the lower end of HF band, which may be considered as the worst scenario.

The scattering patterns are enveloped by the sinc function

$$f(\theta, \phi; \theta_i, \phi_i) = |\text{sinc}(\bar{w}(\sin\theta \sin\phi + \sin\theta_i \sin\phi_i))|$$

$\theta_i, \theta \in (0, \pi/2)$, $\phi_i, \phi \in [0, 2\pi)$, which is common to all $\Delta_{bN}^{a(d,i,s)}$ terms as seen in Appendix A. This envelope brings about the following distinctive features:

(i) The scattered fields diminish dramatically as $\bar{w}|\sin\theta \sin\phi + \sin\theta_i \sin\phi_i|$ raises to 1 and beyond, which addresses a pencil-beam main lobe.

(ii) The following symmetries in azimuth and elevation patterns are observed:

$$f(\theta, \phi; \theta_i, \phi_i) = f(\theta, 2\pi - \phi; \theta_i, \phi_i) = f(\theta, \phi; \theta_i, 2\pi - \phi_i) \tag{12a}$$

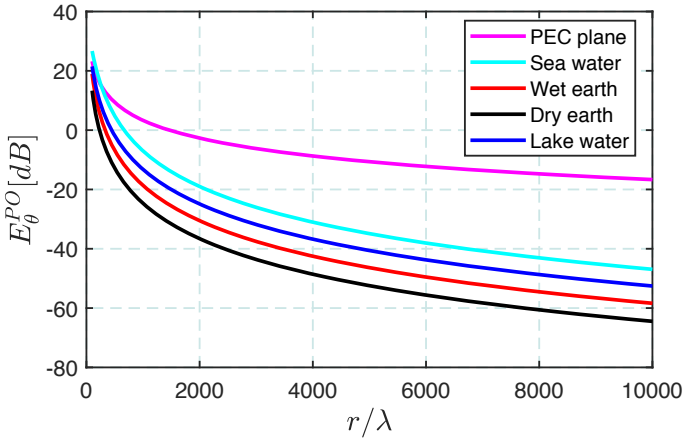

Figure 13. E_θ^{PO} [dB] for $r/\lambda \in (10^2, 10^4)$ and $\theta = \pi/2$ at $f_{\text{MHz}} = 300$.

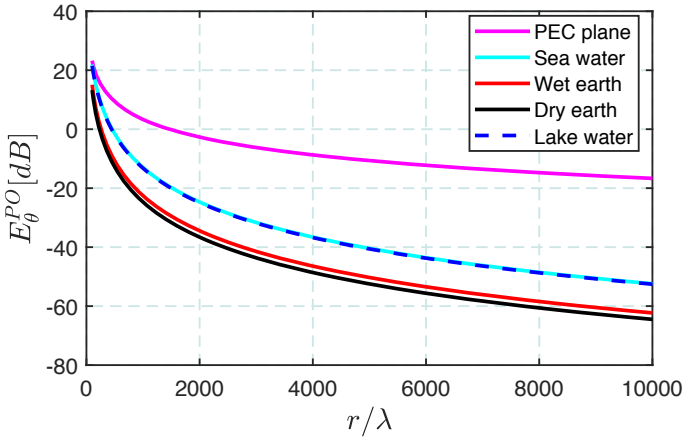

Figure 14. E_θ^{PO} [dB] for $r/\lambda \in (10^2, 10^4)$ and $\theta = \pi/2$ at $f_{\text{GHz}} = 3$.

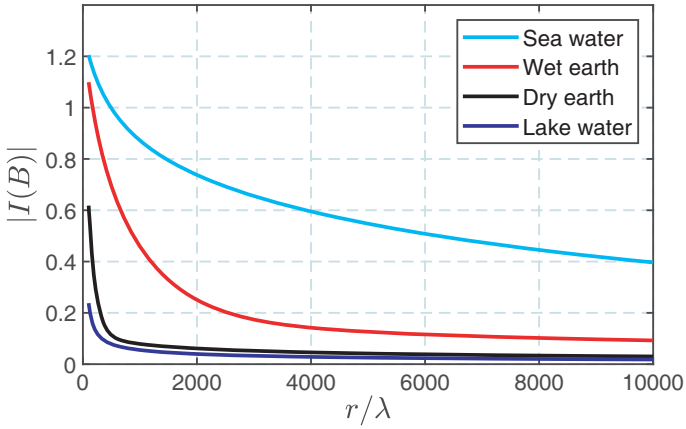

Figure 15. Variations of amplitude of $I(B)$ for $r/\lambda \in (10^2, 10^4)$ and $\theta = \pi/2$ at $f_{\text{MHz}} = 3$.

$$f(\theta, \phi; \theta_i, \phi_i = 0, \pi) = f(\theta, \pi - \phi; \theta_i, \phi_i = 0, \pi) \tag{12b}$$

$$f(\theta, \phi = 0, \pi; \theta_i, \phi_i) = f(\theta, \phi = 0, \pi; \theta_i, \pi - \phi_i) \tag{12c}$$

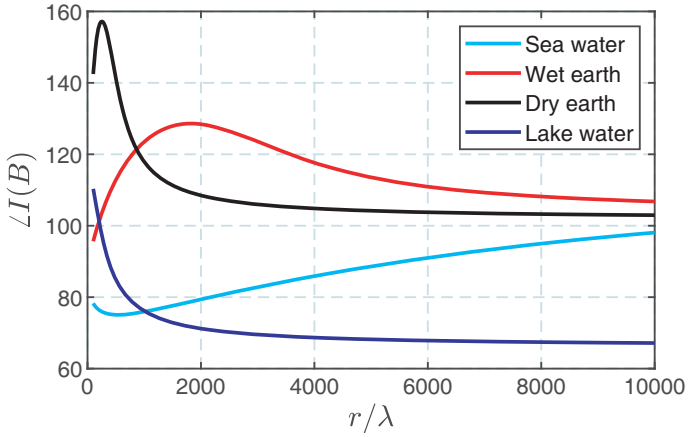

Figure 16. Variations of phase of $I(B)$ for $r/\lambda \in (10^2, 10^4)$ and $\theta = \pi/2$ at $f_{\text{MHz}} = 3$.

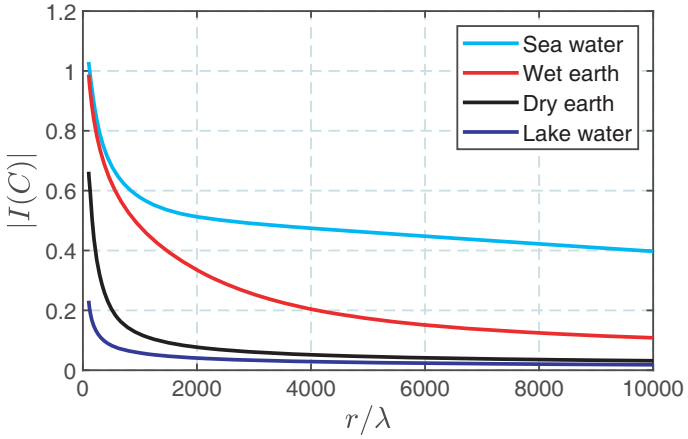

Figure 17. Variations of amplitude of $I(C)$ for $r/\lambda \in (10^2, 10^4)$ and $\theta = \pi/2$ at $f_{\text{MHz}} = 3$.

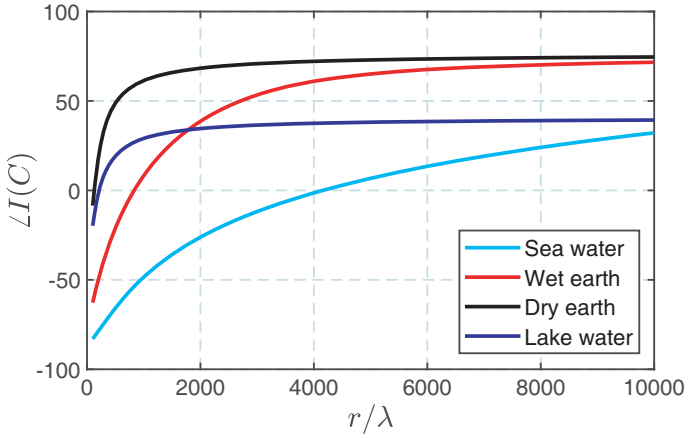

Figure 18. Variations of phase of $I(C)$ for $r/\lambda \in (10^2, 10^4)$ and $\theta = \pi/2$ at $f_{\text{MHz}} = 3$.

Azimuth patterns for E_θ^{PO} [dB] in Eqs. (9a), (10a) are illustrated in Figs. 19–23 in HF-MW band range for $\phi \in [-\pi/2, \pi/2]$. Apart from the aforementioned symmetries in Eq. (12), we observe gradual increase/decrease of amplitude with refractivity/frequency.

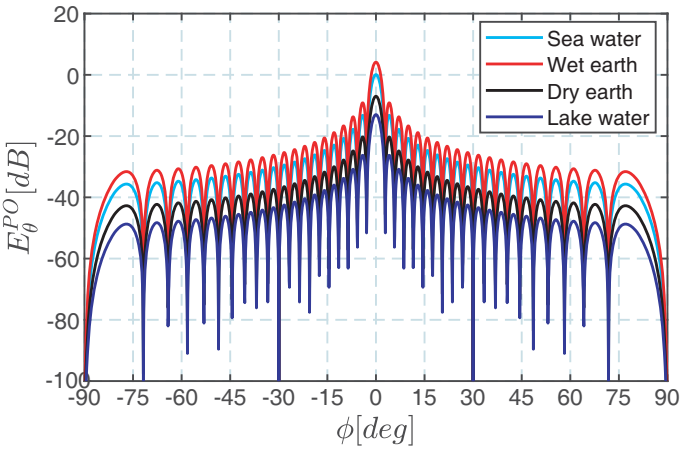

Figure 19. Azimuth pattern of E_θ^{PO} [dB] for $r = 10^3\lambda$, $\theta = \pi/2$ at $f_{\text{MHz}} = 30$.

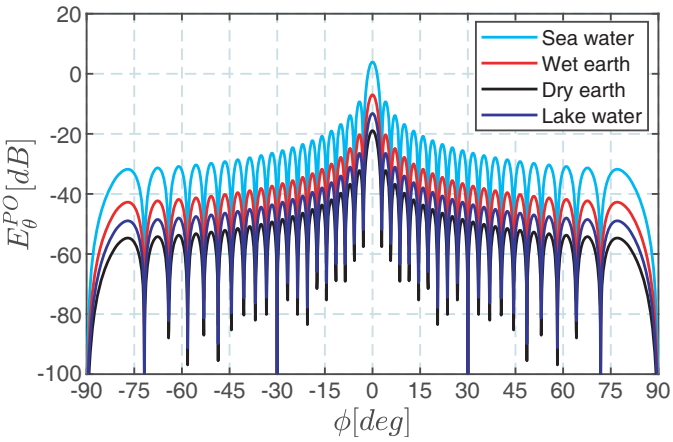

Figure 20. Azimuth pattern of E_θ^{PO} [dB] for $r = 10^3\lambda$, $\theta = \pi/2$ at $f_{\text{MHz}} = 30$.

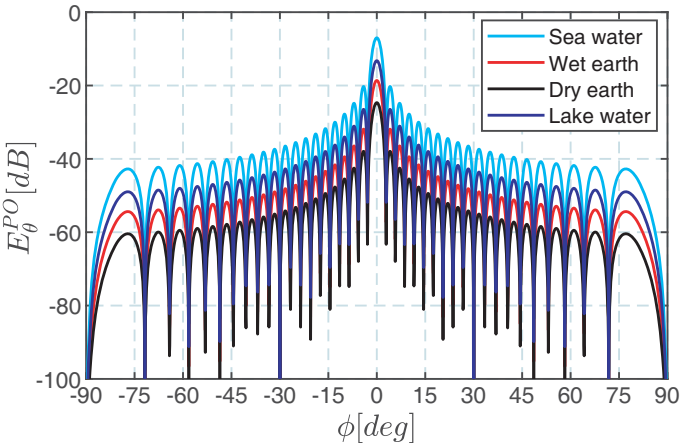

Figure 21. Azimuth pattern of E_θ^{PO} [dB] for $r = 10^3\lambda$, $\theta = \pi/2$ at $f_{\text{MHz}} = 300$.

Finally, the stability of the approximation for RCS^{fs} in Eq. (11) is tackled in Figs. 23–25. In virtue of the wide range of variation of refractivity for the medium parameters (outlined in Table 1) under test, the failure of an exact match of all curves in the far field can be attributed to two items:

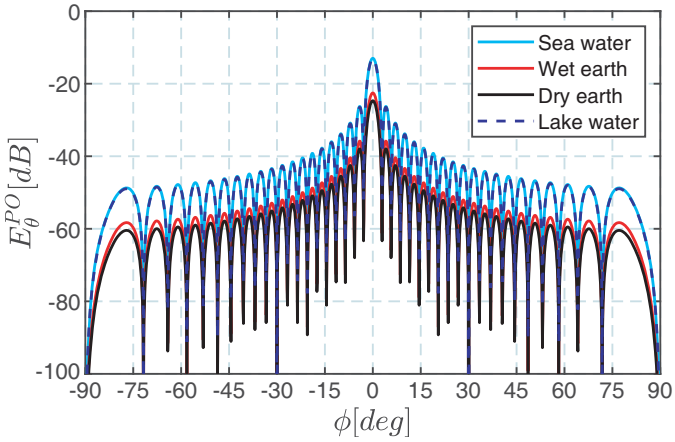

Figure 22. Azimuth pattern of E_θ^{PO} [dB] for $r = 10^3\lambda$, $\theta = \pi/2$ at $f_{\text{GHz}} = 3$.

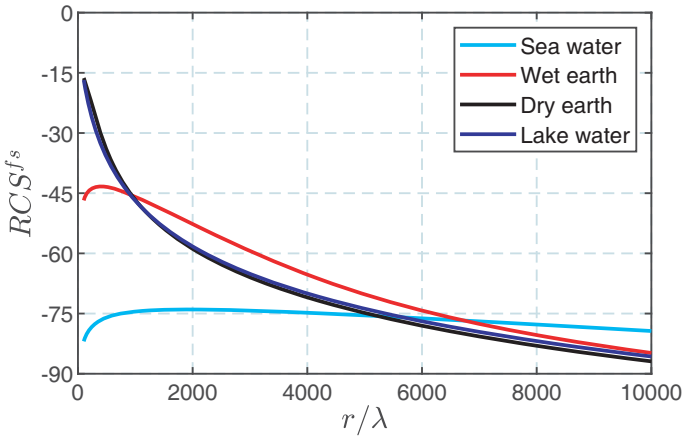

Figure 23. $RCS^{fs}(\theta = \pi/2, \varphi = 0; \theta_i = \pi/4, \varphi_i = 0; f_{\text{MHz}} = 3)$ in (11).

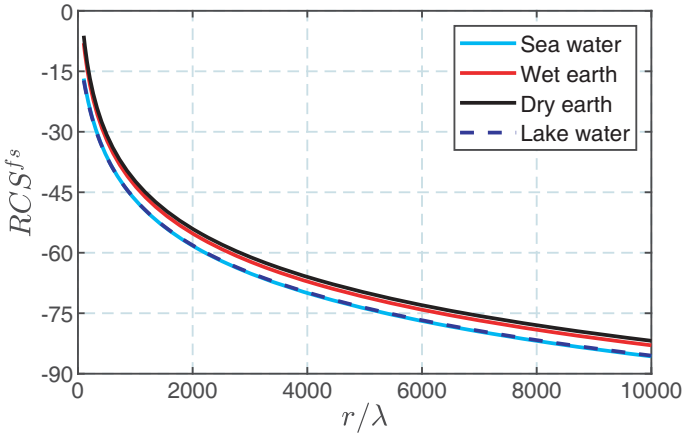

Figure 24. $RCS^{fs}(\theta = \pi/2, \varphi = 0; \theta_i = \pi/4, \varphi_i = 0; f_{\text{GHz}} = 3)$ in (11).

(i) removal of limit operation on r_{RS},

(ii) nonlinear variation of $\Delta_{32}^{2(s)} + \Delta_{33}^{3(s)}$ with r_{RS}.

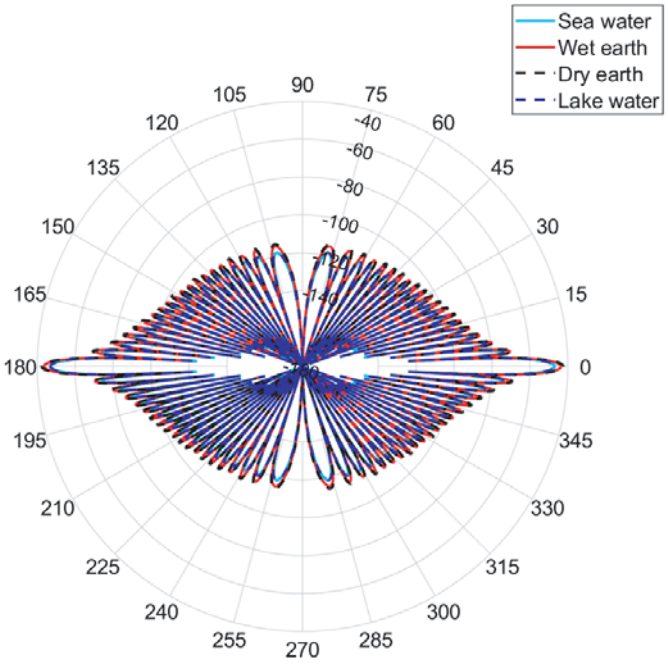

Figure 25. $RCS^{fs}(r = 10^3\lambda, \theta = \pi/2, \varphi \in [0, 2\pi); \theta_i = \pi/4, \varphi_i = 0; f_{\text{GHz}} = 3)$.

The first argument becomes ineffective in the far field. Regarding the second one, the stable (stationary) behaviors of amplitudes and phases of $I(B)$ and $I(C)$ in the far field with increasing frequency should be expected to improve the approximation for RCS^{fs} in (11). This is actually observed in Figs. 23–25. Huge variations in the magnitude of refractivity no more have significant impact on RCS^{fs} information extracted from calculated data at $f_{\text{GHz}} = 3$ and beyond for observations in neither radial nor angular directions.

6. CONCLUDING REMARKS

Analytical solution and numerical illustrations for the problem of plane wave scattering by an electrically large PEC plate located vertically over a simple lossy dielectric half-space are provided. Analytical procedures to extract free space RCS information from measured/calculated data (over planar and spherical transmissive grounds) are introduced by the help of the asymptotic behaviors of surface waves. The success of the numerical tests in Figs. 23–25 is encouraging to continue with actual measurement in MW bands.

As a future work it is also planned to enhance PO approximation by taking into account the edge conditions and the integral equations satisfied by the surface current distribution with the hope to step into complex platforms in advance, based on suitable surface discretization techniques. Relevant works from literature include introducing products of a series of Chebyshev polynomials with functions exhibiting the edge conditions as in [22–24], extension of Singularity Expansion Method in [25], extension of Characteristic Mode Method to PEC plates of arbitrary size in [26], and applications of Galerkin's Method in spectral domain in [27] and [28].

ACKNOWLEDGMENT

This work was supported by Research Fund of the Yildiz Technical University. Project Number: FBA-2019-3691

APPENDIX A. CONTRIBUTIONS BY PARTIAL WAVES TO TOTAL SCATTERED FIELD

In Appendix A, we outline the resultant forms of the *direct*, *perfect image*, and *surface wave* components of the Green dyadic which are required for calculating the scattered electric field. While $\bar{\bar{G}}_d$ and $\bar{\bar{G}}_i$ are evaluated analytically, the surface wave components $\bar{\bar{G}}_s$ are expressed in closed form via the integral $I(\beta)$ discussed in Section IV with

$$A = \sin\theta\sin\phi + \sin\theta_i\sin\phi_i, \quad B = \cos\theta + \cos\theta_i, \quad C = \cos\theta - \cos\theta_i.$$

The Delta values that follow are instrumental not only for the present geometry but also in FF-EFIE formulation of arbitrary platforms.

$$\begin{aligned}
\Delta_{12}^{2(d+i)} &= i\pi\bar{h}\bar{w}\xi_2 E_{\phi 0}\sin^2\theta\sin\phi\cos\phi\sin\theta_i \mathrm{sinc}(\bar{w}A) \\
&\quad \times\left\{\mathrm{sinc}\left(\bar{h}B\right)\left[\exp\left(-i\pi\bar{h}B\right)+R_{TE}\exp\left(i\pi\bar{h}B\right)\right]-\mathrm{sinc}\left(\bar{h}C\right)\left[\exp\left(i\pi\bar{h}C\right)+R_{TE}\exp\left(-i\pi\bar{h}C\right)\right]\right\} \\
\Delta_{12}^{2(s)} &= i\bar{w}E_{\phi 0}\sin^2\theta\sin\phi\cos\phi\sin\theta_i \mathrm{sinc}(\bar{w}A)\frac{1}{N^2}\sqrt{\frac{\pi}{kr}}\frac{e^{i\pi/4}}{\sqrt{2}}\left[\eta_2+\frac{1}{N\sin^3\theta}\left(ikr-\frac{1}{\sin^2\theta}\right)\right] \\
&\quad \times[I(C)-R_{TE}I(B)] \\
\Delta_{13}^{3(d+i)} &= -i\pi\bar{h}\bar{w}\xi_2\sin\theta\cos\theta\cos\phi\mathrm{sinc}(\bar{w}A) \\
&\quad \times\left\{\begin{array}{l}\left[\exp(-i\pi\bar{h}B)\,\mathrm{sinc}(\bar{h}B)+\exp(i\pi\bar{h}C)\mathrm{sinc}(\bar{h}C)\right]\left[E_{\phi 0}\cos\theta_i\sin\phi_i+ZH_{\phi 0}\cos\phi_i\right] \\ +\left[\exp(-i\pi\bar{h}C)\,\mathrm{sinc}(\bar{h}C)+\exp(i\pi\bar{h}B)\mathrm{sinc}(\bar{h}B)\right]\left[R_{TE}E_{\phi 0}\cos\theta_i\sin\phi_i-R_{TM}ZH_{\phi 0}\cos\phi_i\right]\end{array}\right\} \\
\Delta_{13}^{3(s)} &= i\bar{w}\sin\theta\cos\phi\mathrm{sinc}(\bar{w}A) \\
&\quad \times\left\{\begin{array}{l}\pi\bar{h}2\frac{1}{N}\eta_3\times\left\{\begin{array}{l}\exp(i\pi\bar{h}C)\mathrm{sinc}(\bar{h}C)\left[E_{\phi 0}\cos\theta_i\sin\phi_i+ZH_{\phi 0}\cos\phi_i\right] \\ +\exp(i\pi\bar{h}B)\mathrm{sinc}(\bar{h}B)\left[R_{TE}E_{\phi 0}\cos\theta_i\sin\phi_i-R_{TM}ZH_{\phi 0}\cos\phi_i\right]\end{array}\right\} \\ +i\frac{1}{N^2}\sqrt{\pi kr}\frac{e^{i\pi/4}}{\sqrt{2}}\frac{1}{\sin\theta}\times\left\{\begin{array}{l}I(C)\left[E_{\phi 0}\cos\theta_i\sin\phi_i+ZH_{\phi 0}\cos\phi_i\right] \\ +I(B)\left[R_{TE}E_{\phi 0}\cos\theta_i\sin\phi_i-R_{TM}ZH_{\phi 0}\cos\phi_i\right]\end{array}\right\}\end{array}\right\} \\
\Delta_{22}^{2(d+i)} &= i\pi\bar{h}\bar{w}E_{\phi 0}\left[\xi_1-\xi_2\sin^2\theta\sin^2\phi\right]\sin\theta_i\mathrm{sinc}(\bar{w}A) \\
&\quad \times\left\{\mathrm{sinc}(\bar{h}B)\left[\exp(-i\pi\bar{h}B)+R_{TE}\exp(i\pi\bar{h}B)\right]-\mathrm{sinc}(\bar{h}C)\left[\exp\left(i\pi\bar{h}C\right)+R_{TE}\exp(-i\pi\bar{h}C)\right]\right\} \\
\Delta_{22}^{2(s)} &= i\bar{w}E_{\phi 0}\sin\theta_i\,\mathrm{sinc}(\bar{w}A) \\
&\quad \times\left\{\begin{array}{l}\pi\bar{h}2\frac{1}{N}\left[\eta_3\cos\theta-\frac{\eta_1}{N}+\frac{\eta_2}{N}\sin^2\theta\cos^2\phi\right]\left\{\exp(i\pi\bar{h}C)\mathrm{sinc}(\bar{h}C)-R_{TE}\exp(i\pi\bar{h}B)\mathrm{sinc}(\bar{h}B)\right\} \\ -\frac{1}{N^3\sin^3\theta}\frac{e^{i\pi/4}}{\sqrt{2}}\left[ikr\sin^2\theta\sin^2\phi+\cos^2\phi\right]\left[I(C)-R_{TE}I(B)\right]\end{array}\right\} \\
\Delta_{23}^{3(d+i)} &= -i\pi\bar{h}\bar{w}\xi_2\sin\theta\cos\theta\sin\phi\mathrm{sinc}(\bar{w}A) \\
&\quad \times\left\{\begin{array}{l}\left[\exp(-i\pi\bar{h}B)\,\mathrm{sinc}(\bar{h}B)+\exp(i\pi\bar{h}C)\,\mathrm{sinc}(\bar{h}C)\right]\left[E_{\phi 0}\cos\theta_i\sin\phi_i+ZH_{\phi 0}\cos\phi_i\right] \\ +\left[\exp(-i\pi\bar{h}C)\mathrm{sinc}(\bar{h}C)+\exp(i\pi\bar{h}B)\mathrm{sinc}(\bar{h}B)\right]\left[R_{TE}E_{\phi 0}\cos\theta_i\sin\phi_i-R_{TM}ZH_{\phi 0}\cos\phi_i\right]\end{array}\right\} \\
\Delta_{23}^{3(s)} &= i\bar{w}\sin\theta\sin\phi\mathrm{sinc}(\bar{w}A) \\
&\quad \times\left\{\begin{array}{l}\pi\bar{h}2\frac{1}{N}\eta_3\times\left\{\begin{array}{l}\exp(i\pi\bar{h}C)\,\mathrm{sinc}(\bar{h}C)\left[E_{\phi 0}\cos\theta_i\sin\phi_i+ZH_{\phi 0}\cos\phi_i\right] \\ +\exp(i\pi\bar{h}B)\,\mathrm{sinc}(\bar{h}B)\left[R_{TE}E_{\phi 0}\cos\theta_i\sin\phi_i-R_{TM}ZH_{\phi 0}\cos\phi_i\right]\end{array}\right\} \\ +i\frac{1}{N^2}\sqrt{\pi kr}\frac{e^{i\pi/4}}{\sqrt{2}}\frac{1}{\sin\theta}\times\left\{\begin{array}{l}I\,(C)\left[E_{\phi 0}\cos\theta_i\sin\phi_i+ZH_{\phi 0}\cos\phi_i\right] \\ +I\,(B)\left[R_{TE}E_{\phi 0}\cos\theta_i\sin\phi_i-R_{TM}ZH_{\phi 0}\cos\phi_i\right]\end{array}\right\}\end{array}\right\} \\
\Delta_{32}^{2(d+i)} &= -i\pi\bar{h}\bar{w}\xi_2 E_{\phi 0}\sin\theta\cos\theta\sin\phi\sin\theta_i\mathrm{sinc}(\bar{w}A) \\
&\quad \times\left\{\mathrm{sinc}\left(\bar{h}B\right)\left[\exp\left(-i\pi\bar{h}B\right)+R_{TE}\exp(i\pi\bar{h}B)\right]-\mathrm{sinc}(\bar{h}C)\left[\exp(i\pi\bar{h}C)+R_{TE}\exp(-i\pi\bar{h}C)\right]\right\}
\end{aligned}$$

$$\Delta_{32}^{2(s)} = -i\bar{w}\,E_{\phi 0}\sin\theta\sin\phi\sin\theta_i \mathrm{sinc}\,(\bar{w}A) \times \left\{ \begin{array}{l} \pi\bar{h}\dfrac{2}{N}\eta_3\left\{\exp\left(i\pi\bar{h}C\right)\mathrm{sinc}\left(\bar{h}C\right) - R_{TE}\exp\left(i\pi\bar{h}B\right)\mathrm{sinc}\left(\bar{h}B\right)\right\} \\ +i\dfrac{1}{N^2}\sqrt{\pi kr}\,\dfrac{e^{i\pi/4}}{\sqrt{2}}\dfrac{1}{\sin\theta}[I(C) - R_{TE}I(B)] \end{array} \right\}$$

$$\Delta_{33}^{3(d+i)} = i\pi\bar{h}\bar{w}\mathrm{sinc}\,(\bar{w}A)\left[\xi_1 - \xi_2\cos^2\theta\right] \times \left\{ \begin{array}{l} \left[\exp\left(-i\pi\bar{h}B\right)\mathrm{sinc}\left(\bar{h}B\right) + \exp\left(i\pi\bar{h}C\right)\mathrm{sinc}\left(\bar{h}C\right)\right]\left[E_{\phi 0}\cos\theta_i\sin\phi_i + ZH_{\phi 0}\cos\phi_i\right] \\ +\left[\exp\left(-i\pi\bar{h}C\right)\mathrm{sinc}\left(\bar{h}C\right) + \exp\left(i\pi\bar{h}B\right)\mathrm{sinc}\left(\bar{h}B\right)\right]\left[R_{TE}E_{\phi 0}\cos\theta_i\sin\phi_i - R_{TM}ZH_{\phi 0}\cos\phi_i\right] \end{array} \right\}$$

$$\Delta_{33}^{3(s)} = -\bar{w}\mathrm{sinc}\,[\bar{w}A]\,\frac{1}{N}\sqrt{\pi kr}\frac{e^{i\pi/4}}{\sqrt{2}\sin\theta} \times \left\{I\left(C\right)\left[E_{\phi 0}\cos\theta_i\sin\phi_i + ZH_{\phi 0}\cos\phi_i\right] + I\left(B\right)\left[R_{TE}E_{\phi 0}\cos\theta_i\sin\phi_i - R_{TM}ZH_{\phi 0}\cos\phi_i\right]\right\}$$

REFERENCES

1. Michalski, K. A. and J. R. Mosig, "On the surface fields excited by a hertzian dipole over a layered half-space: From radio to optical wavelengths," *IEEE Transactions on Antennas and Propagation*, Vol. 63, No. 12, 5741–5752, 2015.
2. Michalski, K. A. and J. R. Mosig, "The Sommerfeld halfspace problem redux: Alternative field representations, role of Zenneck and surface plasmon waves," *IEEE Transactions on Antennas and Propagation*, Vol. 63, No. 12, 5777–5790, 2015.
3. Michalski, K. A. and D. R. Jackson, "Equivalence of the King and Norton-Bannister Theories of dipole radiation over ground with extensions to plasmonics," *IEEE Transactions on Antennas and Propagation*, Vol. 64, No. 12, 5251–5261, 2016.
4. Michalski, K. A. and R. D. Nevels, "On the groundwave excited by a vertical hertzian dipole over a planar conductor: Second-order asymptotic expansion with applications to plasmonics," *IEEE Transactions on Microwave Theory and Techniques*, Vol. 65, No. 4, 1133–1140, 2017.
5. Sarkar, T. K. and R. F. Harrington, "Radar cross sections of conducting bodies over a lossy half space," *Radio Science*, Vol. 15, No. 3, 581–585, 1980.
6. Anastassiu, H. T., "A closed form, physical optics expression for the radar cross section of a perfectly conducting flat plate over a dielectric half-space," *Radio Science*, Vol. 38, No. 2, 10–1, 2003.
7. Bennani, Y., A. Khenchaf, F. Comblet, and A. Ali-Yahia, "Bistatic Radar Cross Section of a complex target on sea surface," *2010 IEEE International Geoscience and Remote Sensing Symposium*, 2543–2546, Honolulu, HI, 2010.
8. Peng, P. and L. Guo, "A facet-based simulation of the multipath effect on the EM scattering and doppler spectrum of a low-flying target at maritime scene," *IEEE Geoscience and Remote Sensing Letters*, Vol. 15, No. 10, 1495–1499, 2018.
9. Peng, P., L. X. Guo, Q. Gao, and T. Song, "An hybrid scheme for the composite scattering characteristics of a lossy dielectric target above the composite scale sea surface," *2018 International Conference on Microwave and Millimeter Wave Technology (ICMMT)*, 1–3, Chengdu, 2018.
10. Feng, T. and T. Guo, "EM scattering of electrically large target above sea surface with SDFSM-SBR method", *2017 Sixth Asia-Pacific Conference on Antennas and Propagation (APCAP)*, 1–3, 2017.
11. King, R. W. P., M. Owens, and T. T. Wu, *Lateral Electromagnetic Waves: Theory and Applications to Communications, Geophysical Exploration, and Remote Sensing*, Springer Verlag, New York, 1992.
12. Zor, Ö. and B. Polat, "An implementation of King's Green functions in thin wire scattering problems," *ACES Journal*, Vol. 26, No. 12, 1024–1038, 2011.
13. Abramowitz, M. and I. A. Stegun, *Handbook of Mathematical Functions with Formulas, Graphs, and Mathematical Tables*, Dover Publications, 1974.

14. Pouliguen, P., R. Heman, C. Bourlier, J. F. Damiens, and J. Sailard, "Analytical formulae for radar cross section of flat plates in near field and normal incidence," *Progress In Electromagnetics Research B*, Vol. 9, 263–279, 2008.
15. Norton, K. A., "The physical reality of space and surface waves in the radiation field of radio antenna," *Proceedings of the Institute of Radio Engineers*, Vol. 25, No. 9, 1192–1202, 1937.
16. Mclean, Z. S. M. and Z. Wu, *Radiowave Propagation over Ground*, Chapman & Hall, 1993.
17. Houdzoumis, V., "Part I: Scattering of electromagnetic missiles, Part II: Vertical electric dipole radiation over spherical earth," Ph.D. Thesis, Harvard University, Cambridge, MA USA, 1994.
18. King, R. W. P. and C. W. Harrison, "Electromagnetic ground wave field of vertical antennas for communication at 1 to 30 MHz," *IEEE Transactions on Electromagnetic compatibility*, Vol. 40, No. 4, 337–342, 1998.
19. Emery, D. J., D. G. Money, and H. W. Mainwaring, "Some aspects of design and environmental management in HF surface wave radar," *IEE Conference*, 51–55, 2002.
20. Abrarov, S. M., B. M. Quine, and R. K. Jagpal, "A sampling-based approximation of the complex error function and its implementation without poles," *Applied Numerical Mathematics*, Vol. 129, 181–191, 2018.
21. Poppe, G. P. M. and C. M. J. Wijers, "More efficient computation of the complex error function," *ACM Transactions on Mathematical Software (TOMS)*, Vol. 16, 38–46, 1990.
22. Butler, C. and D. Wilton, "General analysis of narrow strips and slots," *IEEE Transactions on Antennas and Propagation*, Vol. 28, No. 1, 42–48, 1980.
23. Butler, C., "Current induced on a conducting strip which resides on the planar interface between two semi-infinite half-spaces," *IEEE Transactions on Antennas and Propagation*, Vol. 32, No. 3, 226–231, 1984.
24. Walker, W. and C. Butler, "A method for computing scattering by large arrays of narrow strips," *IEEE Transactions on Antennas and Propagation*, Vol. 32, No. 12, 1327–1334, 1984.
25. Sun, W., K. M. Chen, D. P. Nyquist, and E. J. Rothwell, "Determination of the natural modes for a rectangular plate (transient scattering)," *IEEE Transactions on Antennas and Propagation*, Vol. 38, No. 5, 643–652, 1990.
26. Wu, Q. and D. Su, "A broadband model of the characteristic currents for rectangular plates," *IEEE Transactions on Electromagnetic Compatibility*, Vol. 55, No. 4, 725–732, 2012.
27. Coluccini, G. and M. Lucido, "A new high efficient analysis of the scattering by a perfectly conducting rectangular plate," *IEEE Transactions on Antennas and Propagation*, Vol. 61, No. 5, 2615–2622, 2013.
28. Lucido, M., "Electromagnetic scattering by a perfectly conducting rectangular plate buried in a lossy half-space," *IEEE Transactions on Geoscience and Remote Sensing*, Vol. 52, No. 10, 6368–6378, 2014.